5 Results & Discussion

5.1 Surface roughness generation under influence of a minimum undeformed chip thickness

As shown in Section 2.1.3 the surface topography of turned surfaces is accessible to a discrete mathematical description for certain process parameters - in particular at high feed rates. The difficulty in using Equation 4 or Equation 5 is that they were only created for tools with a defined corner radius but no other features. Although it is possible to create formulae to express surface finish parameters (such as R_t) for other tool geometries this would be a rather inflexible approach.

Nevertheless it makes sense to examine Brammerz's equation (see Equation 5) in more detail and compare its predictions to some initial experimental results. Starting from the simplified version of the equation and assuming constant conditions for the cutting tool (cutting edge and corner radii) it is possible to express surface roughness R_t as a function of feed f.

$$R_t = \frac{f^2}{8 \cdot r_\varepsilon} + \frac{h_{min}}{2} \cdot \left(1 + \frac{r_\varepsilon \cdot h_{min}}{f^2}\right)$$

or

$$R_t = \frac{1}{8 \cdot r_\varepsilon} f^2 + \frac{h_{min}}{2} + \frac{r_\varepsilon \cdot h_{min}^{\ 2}}{2} \cdot \frac{1}{f^2}$$

this can be written as:

Equation 9:

$$R_t(f) = c_1 \cdot f^2 + c_2 + c_3 \cdot \frac{1}{f^2}$$

with $c_1 = \frac{1}{8 \cdot r_\varepsilon}$; $c_2 = \frac{h_{min}}{2}$; $c_3 = \frac{r_\varepsilon \cdot h_{min}^{\ 2}}{2}$

From Equation 9 it is apparent that Brammerz's formula is the sum of quadratic, a constant and a hyperbolic term. For small absolute values of f the quadratic term will approach zero, whereas the hyperbolic term will approach infinity. As a result the sum of the three terms will also approach infinity for small values of f. Clearly infinite surface roughnesses do not occur in reality, therefore a better estimate of achievable surface finish at low feed rates must be made. Upon examination of the argument made in [10] the minimum point of the function can be determined:

Equation 10:

$$R_{t,min} = h_{min}$$
$$f_{min} = \sqrt{2 \cdot r_\varepsilon \cdot h_{min}}$$

Although the behaviour of the function is described in the paper and experimental results are shown, which seem to confirm the rise in surface finish at low feed rates, no explanation is given as to why this should occur. One of the possibilities, which could explain this phenomenon, is an increased tendency of the cutting tool to chatter. However it is not possible to explain this phenomenon by using the argument of a minimum undeformed chip thickness. The effect of chatter and other asynchronous error motions will be examined in chapter 5.3.3.

It is possible to refine Equation 5 and thus avoid an increase in predicted roughness (also see Figure 20):

Equation 11: $$R_t(f) = \begin{cases} \dfrac{f^2}{8 \cdot r_\varepsilon} + \dfrac{h_{\min}}{2} \cdot \left(1 + \dfrac{r_\varepsilon \cdot h_{\min}}{f^2}\right) & \text{for } f > \sqrt{2 \cdot r_\varepsilon \cdot h_{\min}} \\ h_{\min} & \text{for } f \le \sqrt{2 \cdot r_\varepsilon \cdot h_{\min}} \end{cases}$$

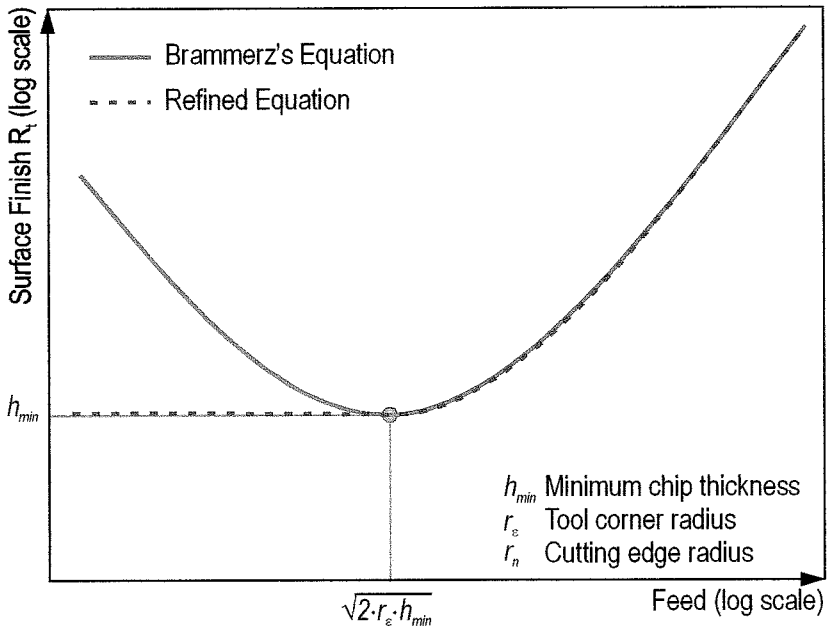

Figure 20: Comparison of Brammerz's equation and Equation 11

In order to verify the above 'refined equation' and to arrive at a more generic and versatile surface roughness prediction a computer program was created to numerically simulate the surface generation. The program calculates a two-dimensional surface topography for any tool profile and cutting path, which can be described as a set of data points or by discrete equations.

A flow chart of the program in shown in Figure 21. In order for the program to work the cutting conditions must be defined. The macroscopic tool profile can be defined for example by its radius. It is also possible to superimpose serrations on the tool profile to simulate the effect of wear marks on the tool. It is also possible to read-in data from profile measurements carried out on real cutting tools.

The initial surface topography and the tool path must also be defined. Initially they are treated at perfect straight lines, but modifications are made to the tool path in later chapters.

The initial cutting conditions are fed into the machining module of the software. The cutting tool is incremented along the cutting path by the feed rate. The common area of the cutting tool and work surface is determined and the chip profile is calculated as a function of the position on the cutting edge.

Subsequent algorithms use the undeformed chip thickness as an input to determine the amount of material removed along the cutting edge. The machined surface is created by repeatedly incrementing the cutting tool position by the feed along the cutting path.

Finally the simulated machined surface can be plotted on a graph or examined by calculating its surface finish parameters.

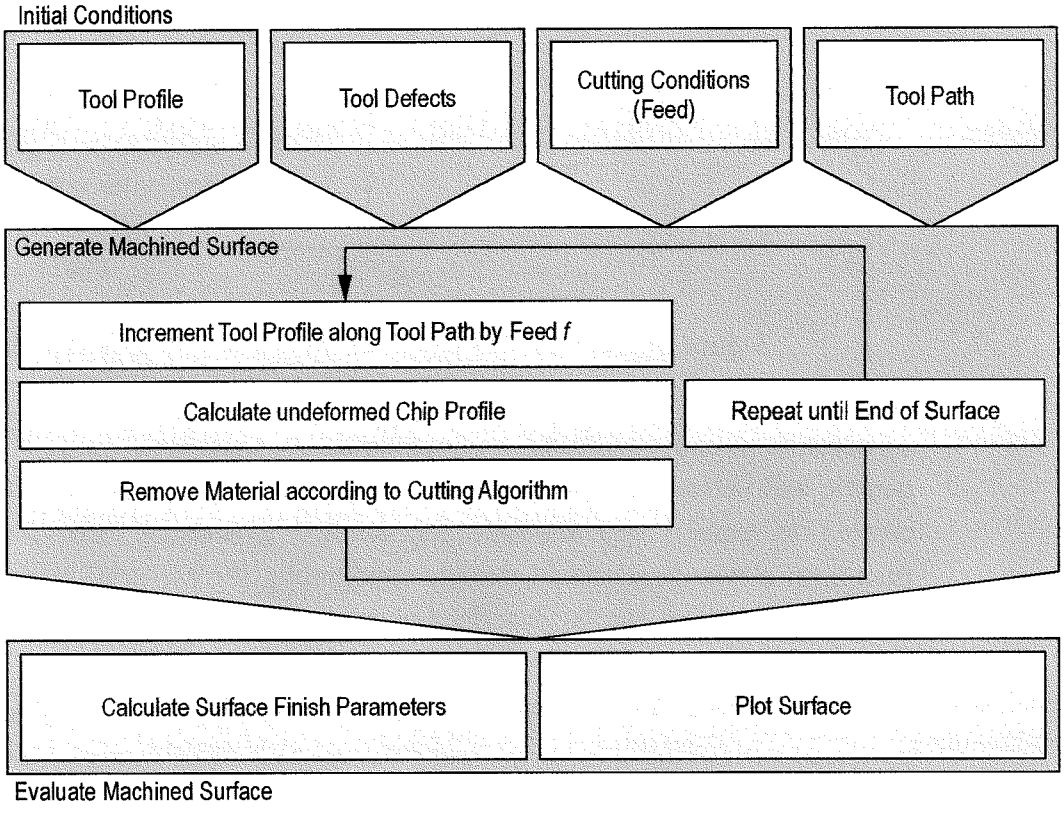

Figure 21: Flow Diagram of Surface Generation Software

Using the computer program described above the surface finish generated by cutting tool was simulated according to the minimum undeformed chip thickness theory.

The undeformed chip profile is determined by iteratively calculating the distances between points on the work piece profile and the current tool profile overlapping with the work piece. The minimum distance for each point on the work piece surface and the corresponding co-ordinates of the point on the cutting tool profile are saved for further evaluation.

The cutting algorithm itself uses the chip profile data to determine material removal from the work piece surface. For each local undeformed chip thickness the removal function can be expressed as the sum of different mechanisms. Contributing to the changes to the work piece profile are actual chip removal, plastic deformation, and elastic deformation. As such a material partition equation can be formulated as:

Equation 12: $$h(x) = h(x) \times \left[p_{chip}(x) + p_{plastic}(x) + p_{elastic}(x) + \varepsilon \right]$$

with

$h(x)$: local undeformed chip thickness

$p_{chip}(x)$: relative chip removal

$p_{plastic}(x)$: relative plastic deformation

$p_{elastic}(x)$: relative elastic deformation

ε: residual error

The conventional terms for elastically or plastically deformed proportions of the undeformed chip thickness can be expressed in terms of the material partition equation as follows:

Equation 13: $$\Delta h_{el}(x) = h(x) \times p_{elastic}(x)$$

and

$$\Delta h_{pl}(x) = h(x) \times p_{plastic}(x)$$

With Equation 12 the local undeformed chip thickness is expressed as being constituted by the above factors (plus an error term). The local undeformed chip thickness as well as the contributing terms are expressed as functions of 'x' as they change with the position on the work piece surface. 'x' is the horizontal co-ordinate on the work piece surface parallel to the straight feed motion.

Obviously the term in the square brackets has to be equal to one to satisfy the equation. Despite the fact that there are known errors such as material side flow in hard turning they are assumed at this stage to be very small and can therefore be neglected. As a result:

Equation 14: $$p_{chip}(x) + p_{plastic}(x) + p_{elastic}(x) = 1$$

Depending on this material partition it is possible to determine the chip removal at any given point and therefore calculate the shape of the work piece surface after material removal has taken place.

The difficulty with this equation is in determining the relative contribution that each factor has at a given position. In some cases this is made more convenient by describing the factors as functions of undeformed chip thickness rather than as functions of location (Equation 15) as most theoretical examinations work with the undeformed chip thickness parameter.

Equation 15: $$p_{chip}(h)+p_{plastic}(h)+p_{elastic}(h)=1$$

However changing the co-ordinate in which the factors are calculated does not in itself solve the task of attributing the right magnitudes to each factor. In particular differentiating between complete chip removal and complete plastic deformation can be difficult as both lead to the same work piece topography.

Following on from the initial evaluation made of Brammerz's theory the underlying mechanism can be assessed with the method described above and the surface roughness can be simulated. Brammerz stated that no chip removal takes place below the minimum undeformed chip thickness h_{min}. Furthermore the assumption is made that the chip below the minimum undeformed chip thickness does not undergo plastic deformation as the remaining surface roughness R_t is – at best – equal to the minimum undeformed chip thickness.

No statement is made about plastic deformation in the segment of the chip where material removal takes place, but for simplicity reasons the assumption shall be made that no plastic deformation takes place in this region of chip either. The surface profile resulting from the simulation will not be affected by this assumption. As there is an instantaneous transition from chip removal to elastic deformation in Brammerz's work the proportional contributions of the material partition equation can be expressed as follows (also see Figure 22):

Equation 16:
$$p_{chip}(h)=\Phi(h-h_{min})$$
$$p_{plastic}(h)=0$$
$$p_{elastic}(h)=\Phi(h_{min}-h)$$

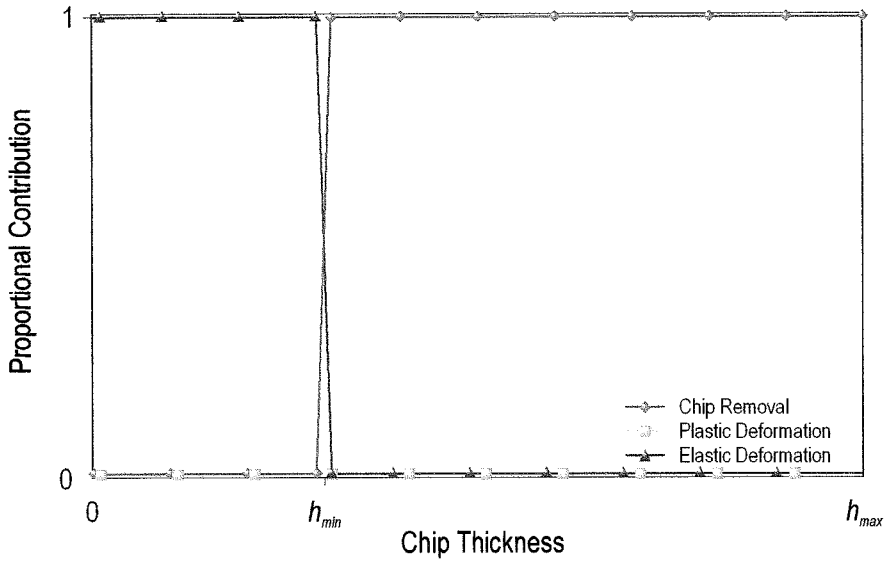

Figure 22: Proportional contribution to material removal in Brammerz's theory

The results of this simulation can be seen in Figure 23. Also shown in the same figure is the graph created by Brammerz's original formula. The graphs were created for a cutting tool with a corner radius of $r_\varepsilon = 0.4$mm and a minimum undeformed chip thickness $h_{min} = 0.9369\mu m$[4]. For other corner radii and undeformed chip thicknesses the graph changes its scaling and position in the co-ordinate system. However the fundamental differences still apply in the same way.

As can be seen in Figure 23 the computer simulated roughness (R_t) and Brammerz agree very well for higher feed rates (see Zone 1). If there are differences in the two graphs then they are purely a cause of the numerical inaccuracies in the different methods of calculation. At the minimum point for the Brammerz equation (see Equation 10) both curves reach $R_t = h_{min}$ as predicted.

[4] The value of $h_{min} = 0.9369\mu m$ is calculated using Equation 7 with a cutting edge radius $r_n = 10\mu m$ and $\Theta = 25°$

Decreasing feed from there onwards leads to the rise in the Brammerz equation discussed earlier in this section. In contrast the simulated roughness R_t remains at approximately, but not exactly, h_{min} (Zone 2). Contrary to what has been assumed in Equation 11 and Figure 20 this levelling of the surface roughness does not stay the same for all small feed rates. Below a feed rate of $f \approx 12 \times h_{min}$ the simulated roughness enters a region of instability (Zone 3). In this range of feeds the simulated roughness is characterised by small regions of low surface roughness alternating with similar regions where the surface roughness R_t is approximately equal to the minimum undeformed chip thickness h_{min}.

The shape of the graph in this area remains the same even if the tool corner radius or the minimum undeformed chip thickness change. The scaling and the position of the graph however is affected by these changes

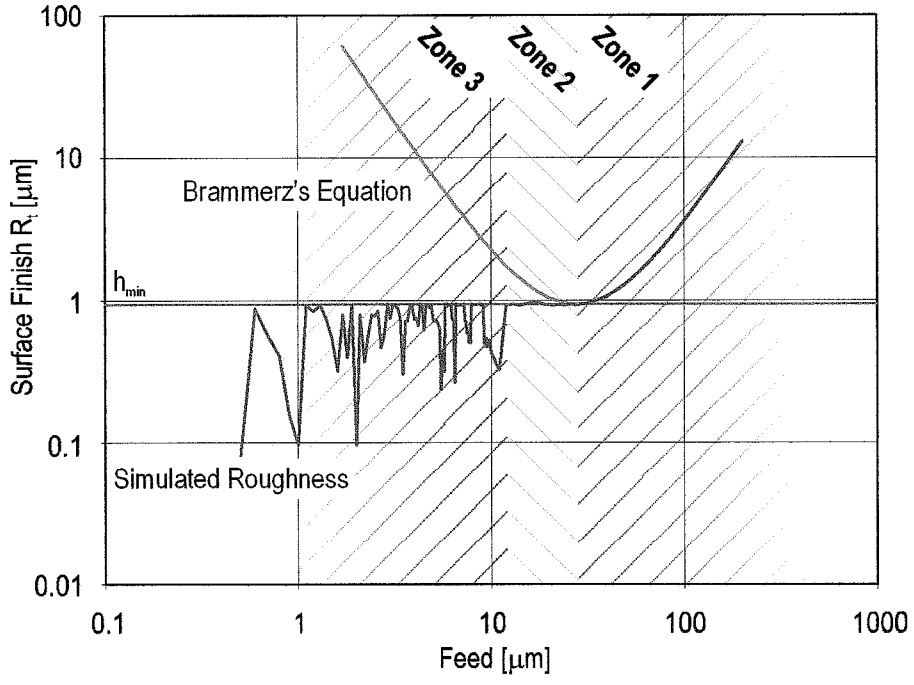

Figure 23: Comparison of Brammerz's and simulated roughnesses

In order to understand how the simulated roughness pattern in Zone 3 occurs it is necessary to look at the development of the turned surface over several revolutions of the work piece. A schematic development over six revolutions of a work piece can be seen in Figure 24.

For the first revolution the cutting tool plunges into the work piece and the chip is removed, resulting in a perfect imprint of the cutting tool in the work piece surface. For this cut the effect of the minimum undeformed chip thickness is ignored. In the second revolution the cutting tool is incremented along the tool path by one feed increment. The undeformed chip profile is split into two areas: one where the undeformed chip thickness h is larger than the minimum undeformed chip thickness h_{min}, and a second one where h is smaller than h_{min}. In the former area the full undeformed chip thickness is removed, whereas in the latter area the work piece surface remains unchanged.

During the third revolution the tool is incremented again. This time the undeformed chip profile shows an highly non-uniform profile in the location where during last revolution the transition in undeformed chip thickness from smaller to larger than h_{min} occurred. As a result of this the undeformed chip profile is now divided into four areas: in two a chip is removed, in the other two the work piece surface remains unchanged.

As this is repeated over the next revolutions the undeformed chip profile is greatly influenced by the chip removal of previous revolutions. In spite of this a steady state establishes itself after a few revolutions of the work piece. The start of this can be seen during the fourth, fifth and sixth revolution. It is important to note that the surface roughness R_t of the steady state profile is significantly smaller than the minimum undeformed chip thickness h_{min}.

The outcome of the profile generated by turning at low feed rates is dependent on the multiples of feed, minimum undeformed chip thickness and the way the areas of alternating chip removal are spaced along the undeformed chip profile. Very small changes in either feed or minimum undeformed chip thickness can lead to roughnesses R_t, which are either approximately equal to h_{min} or significantly smaller.

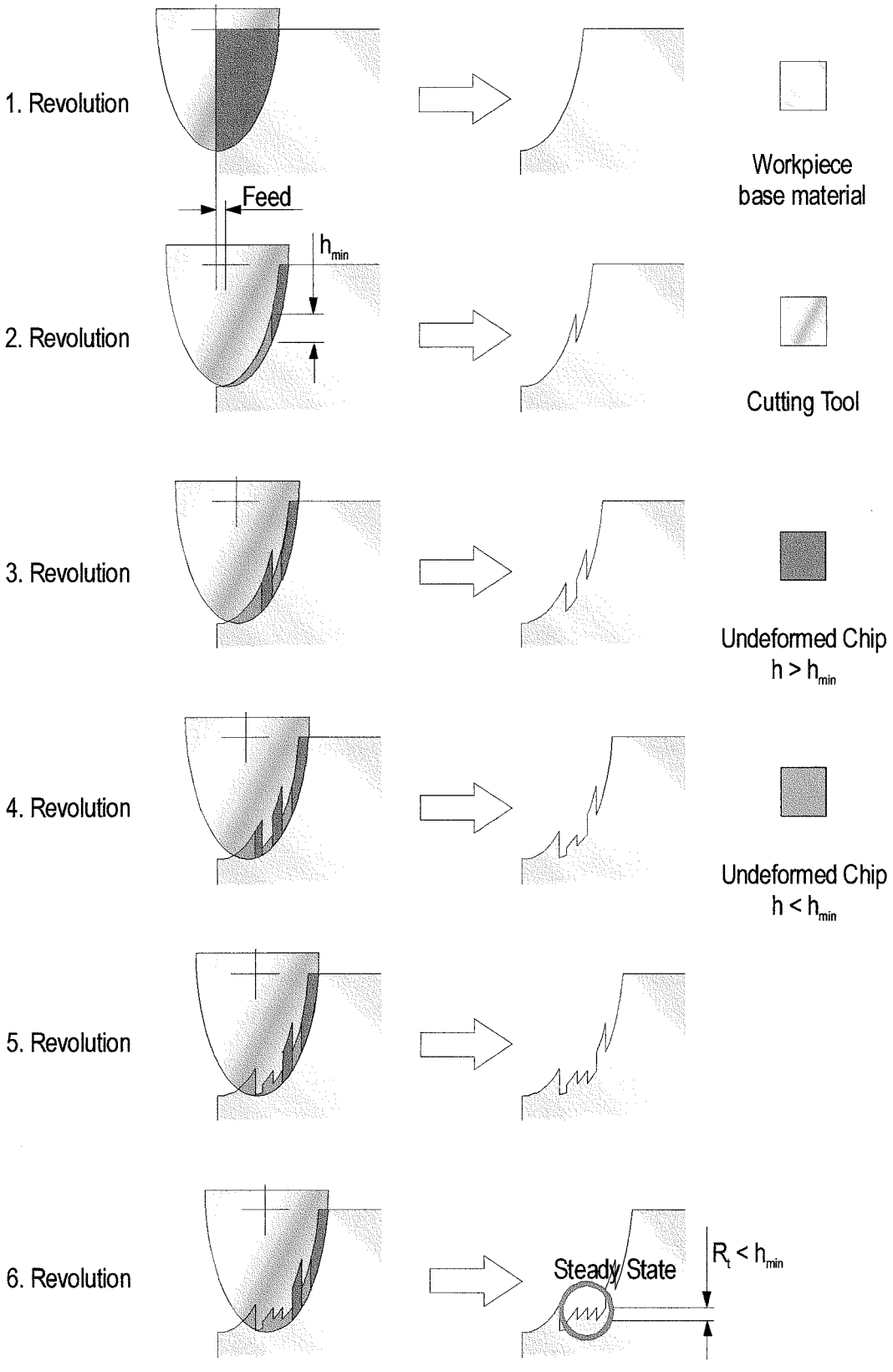

Figure 24: Simulated development of surface roughness at low feed rates (diagrams greatly magnified in the vertical direction)

Different surface profiles, which are theoretically generated by turning according to the computer simulation of Brammerz's theory are shown in Figure 25. All profiles in this figure are calculated based on a tool corner radius of $R_\varepsilon = 0.4$mm and a minimum undeformed chip thickness of $h_{min} = 0.9369$µm.

At higher feed rates down to approximately 50µm the surface profile exhibits the grooved shape typical for turning. The transition to chip removal when the minimum undeformed chip thickness is overcome can clearly be identified by the vertical sections of the cusps. This effect becomes less pronounced at higher feeds. Although the length of the vertical tear-off remains constant, the overall height of the profile increases with higher feeds, thus making the tear-off less important. This behaviour corresponds with 'Zone 1' in Figure 23.

At a feed rate of 30µm the rounded grooves are still visible, but now they are highly non symmetrical with the vertical tear-off of similar size as the total profile height. This behaviour occurs at the minimum point of the Brammerz curve and at the transition from 'Zone 1' to 'Zone 2' in Figure 23.

With decreasing feed (20µm and 15µm) the groove making up the surface profile becomes less and less rounded, although the profile height remains approximately the same. At $f = 15$µm the effect of multiple areas of chip removal (as illustrated in Figure 24) can be seen. This range of feed rates correspond to 'Zone 2' in Figure 23.

At a feed of $f = 12$µm the transition from 'Zone 2' to 'Zone 3' is reached. The surface profile is characterised by regular high and narrow structures, which are bounded by vertical tear-offs. In between these structures the imprint of the cutting edge can still be seen.

Decreasing the feed further reduces the width of these structures very quickly, until they disappear ($f = 11$µm). At this stage a significant reduction of profile height can be observed. The simulated surface roughness drops from $R_t = 0.92$µm to $R_t = 0.32$µm - nearly a threefold improvement.

As discussed earlier further reductions in feed do not automatically yield improvements in surface roughness.

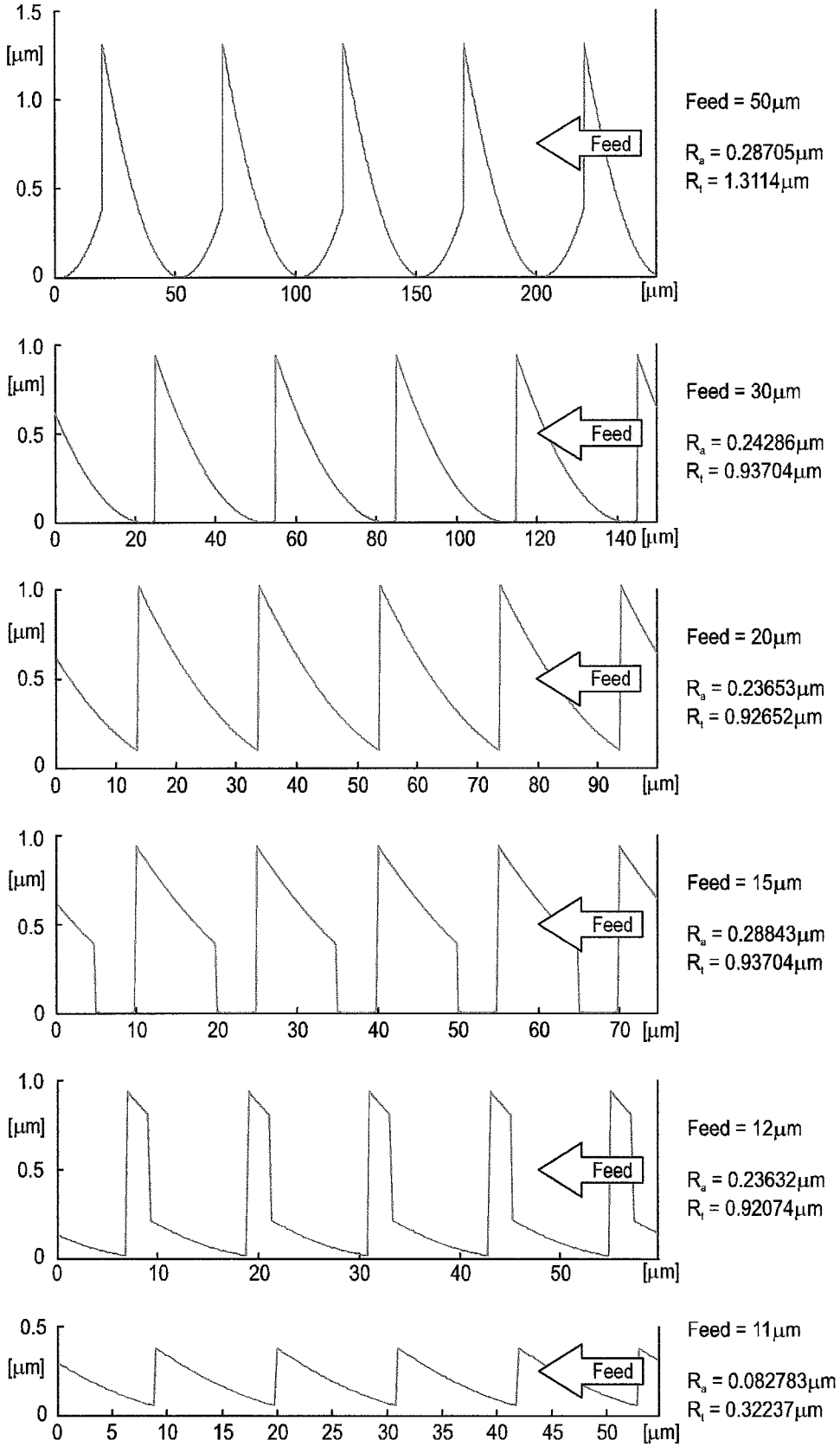

Figure 25: Simulated surface profiles using Brammerz at low feeds

5.1.1 Comparison of actual and simulated profiles

When comparing even a small set of experimental results with simulated surfaces it becomes obvious that the simulation with a minimum undeformed chip thickness gives rather pessimistic results. Figure 26 shows the simulated average roughness (R_a) for a cutting tool with a tool corner radius $r_\varepsilon = 0.4$mm. Experiments were conducted at a cutting speed of $v_c = 140$m/min. For the simulation a cutting edge radius of $r_n = 10\mu$m has been assumed. This is the lower figure typically quoted by CBN cutting tool manufacturers. While at higher feed rate ($f = 100\mu$m), there is reasonably good agreement between simulated and measured roughness, at the lower feed rates of $f = 5\mu$m and $f = 50\mu$m, the measured results are at least two times better than the computer prediction. It is also notable that at the feed rate of $f = 5\mu$m the experimental results are very repeatable, even though they have been obtained with different cutting tools. From the unsteady behaviour of the surface finish prediction a much greater variability was to be expected.

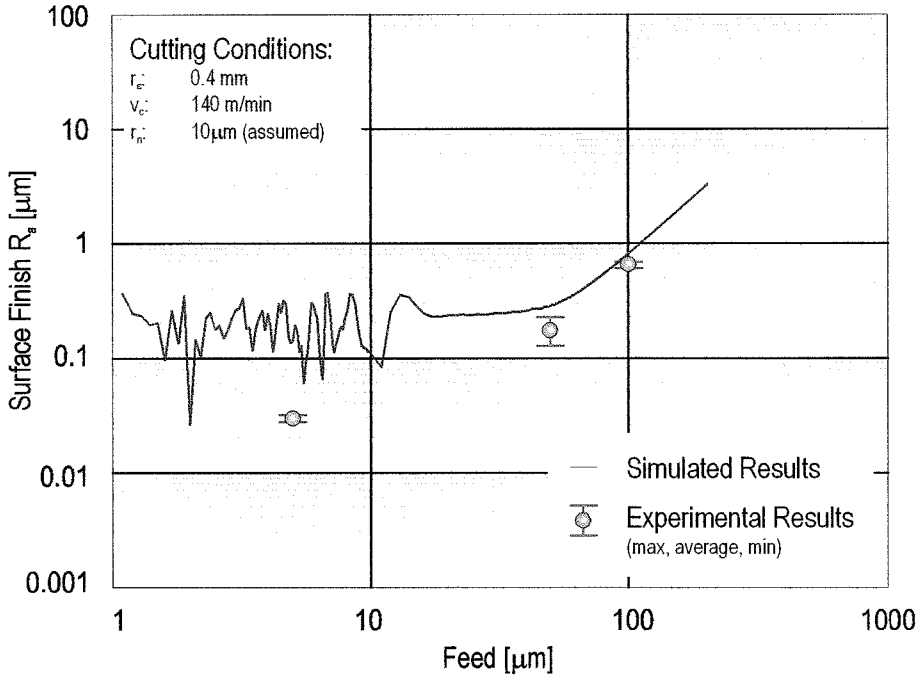

Figure 26: Comparison of simulated and actual surface roughness (R_a)

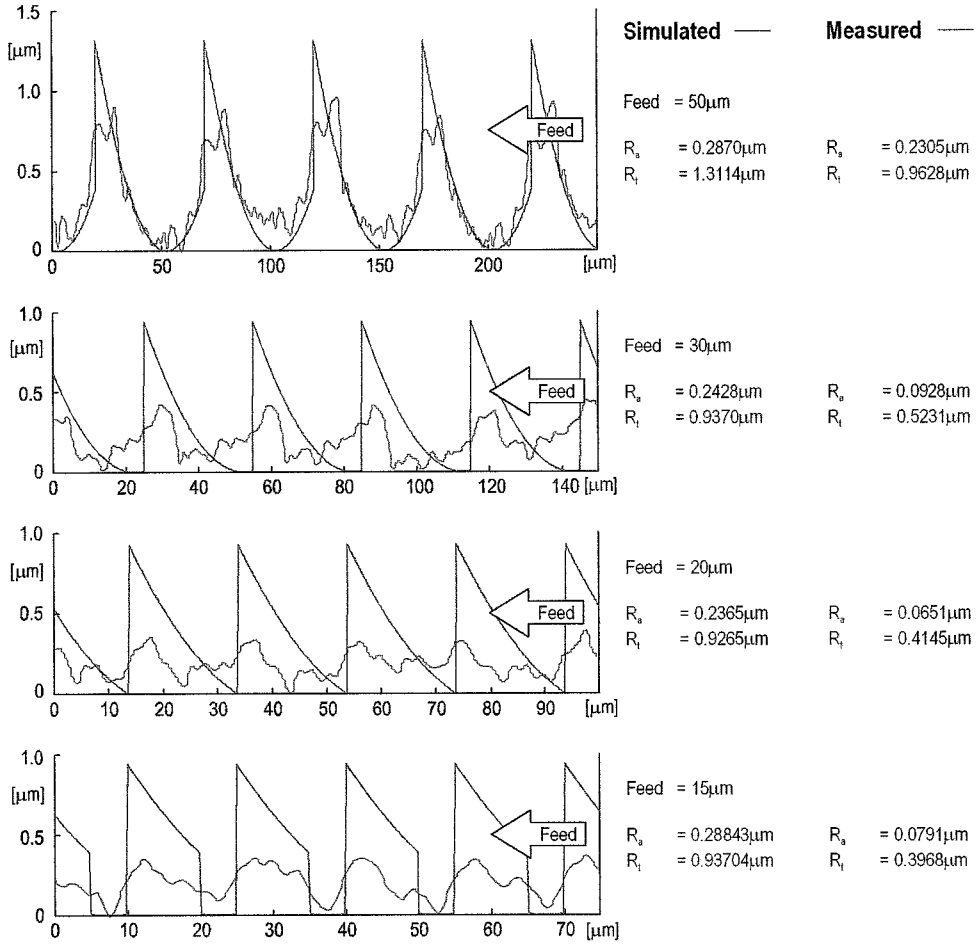

Figure 27: Comparison of simulated and actual surface profiles (r_ε=0.4mm, r_n=10µm[5])

Figure 27 shows a comparison of simulated and actual surface profiles as measured on a Form Talysurf. While at f = 50µm the two surface profiles are quite similar, for the lower feed rates in the figure important discrepancies between simulation and actual profile can be seen: In terms of the numerical roughness parameters the simulated results are 2 - 2.5 times worse than the measured results. Not only that but also the shapes of the profiles are distinctly different. It should be kept in mind that the roughnesses given here are calculated from levelled raw data as outlined in Section 4.3. The strong asymmetry of the simulated profiles, which is caused by the vertical tear-off of the chip, cannot be seen in the recorded traces. In fact the recorded traces seem to be rounded grooves down to feed rates of f = 15µm or lower.

[5] Estimated figure for surface roughness simulation

5.2 Simulation of surface roughness generation at low feed rates with imperfect cutting tools

In the light of the results discussed in the previous chapter, the question has to be asked whether the minimum undeformed chip thickness theory applies in hard turning and whether there is a better model for predicting surface roughness. This is particularly so as other researchers have reported previously that there is a very good correlation between the shape of the feed mark and the cutting tool topography in hard turning [21], [59].

For subsequent simulations the material partition equation was simplified to:

Equation 17:
$$\begin{aligned} p_{elastic} &= 0 \\ p_{chip}(h) + p_{plastic}(h) &= 1 \end{aligned}$$

Because plastic deformation and chip removal have the same effect on surface topography it is not necessary at this stage to determine to what degree the surface is created by which respective mechanism. Due to this fact the actual material partition equation used in the cutting algorithm in most of the simulations was simply:

Equation 18: $p_{chip} = 1$

Doing this also allows great simplification of the computer program which simulates the surface roughness generation and reduces computation times very significantly.

So far the assumption in the simulations has been made that the cutting edge geometry is a perfect circular arc of a defined radius. Measuring tool profiles of unused CBN cutting tools reveals that this is by no means the case. Figure 28 shows a typical cutting tool profile. It is clearly visible that the cutting edge radius is far from perfect. On the lowest region of the profile, where the actual cutting takes place, peaks and valleys of height (or depth) in the order of 0.4µm and a width of around 8µm can be seen. The exact shape and size of both macro- and micro-geometry of the active area of a cutting tool not only changes from tool to tool, it also is greatly affected by the wear condition of the cutting tool.

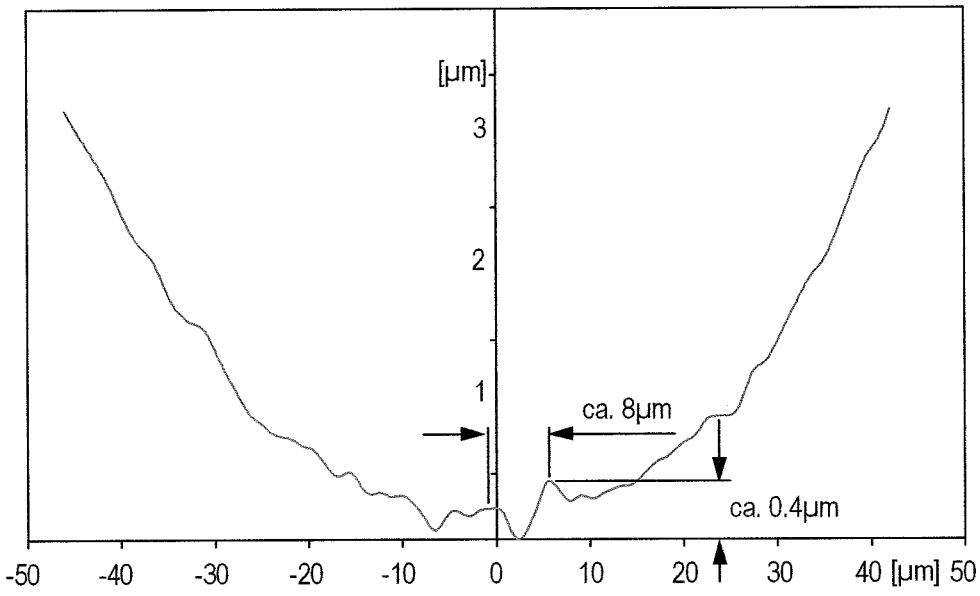

Figure 28: Profile of an unused CBN cutting tool (r_ε=0.4mm, BNX25)[6]

In order to test the effect which the presence of small ridges on the cutting edge will have the simulation of surface generation was carried out with imperfect cutting tool profiles.

5.2.1 Simulation of single-defect cutting edges

For the simulation of the effect which single defects on cutting edges have, two principle defect geometries were chosen. One was a sharp edged isosceles triangle centred on the lowest point of the cutting edge profile. Also used was a circular arc of defined profile height and radius. The height and radius of the circular profile were selected first, the width of the triangular defect was then matched to the same resulting defect width (see Table 7). The two different defect profiles were used both in a convex and a concave configuration (see Figure 29).

Radius of Circular Profile	Profile Height (Both Profiles)	Corresponding Profile Width
2µm	0.08µm	1.12µm
5µm	0.20µm	2.80µm
8µm	0.25µm	3.97µm

Table 7: Defect dimensions used in the simulation

[6] Tool profiles were measured with the Form Talysurf. Measuring characteristics given in Table 5 apply.

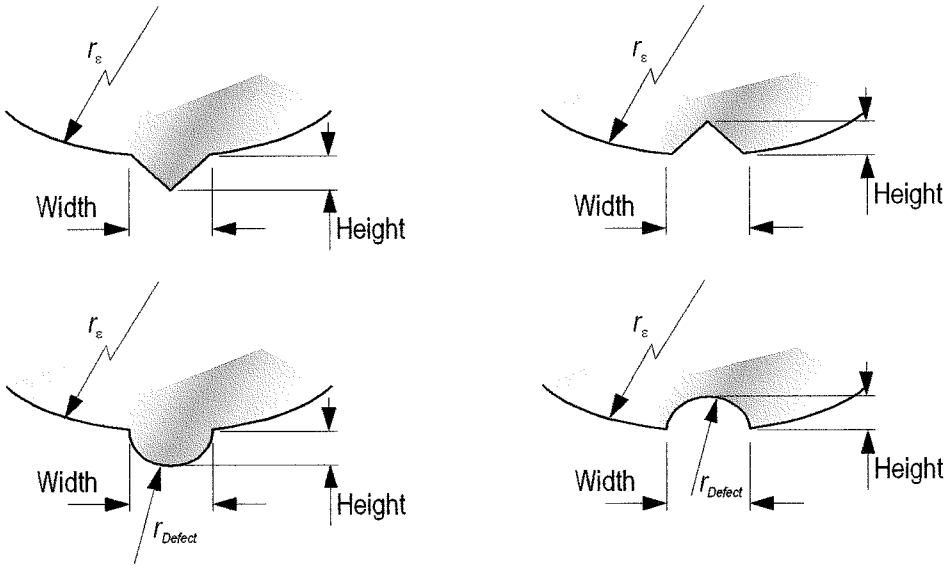

Figure 29: Tool profiles with single defects

The simulated results of generating surfaces with cutting tools with a single edge defect are shown in Figure 30. All results are shown for peak-to-valley-roughness (R_t). In addition to the simulated results the kinematic roughness of defect-free cutting tools (according to Equation 4) are shown as the diagonal lines in the graphs.

At high feed rates the surface roughnesses generated with imperfect tool profiles are approximately equal to those generated with Equation 4. The defects still have a certain effect on the roughness, but as the defect size is small in comparison to the overall roughness the effect is negligible (① in Figure 30).

As feed decreases and the surface roughness approaches the defect height, the roughness prediction with imperfect cutting edges deviates from Equation 4, to form a plateau on which the surface roughness is approximately equal to the defect height (②). While there is little difference in whether the defect geometry is triangular or circular at this stage, there is a marked difference between convex and concave profiles. The progression onto the plateau happens gradually for convex defect shapes, in fact tools with a convex defect profile change from a seemingly asymptotic behaviour in ① to a real asymptotic behaviour in ②.

For concave profiles there is an instant change in behaviour in the transition from ① to ②. Initially the roughness predictions follow almost precisely Equation 4, the cutting tools behave as if there was no defect at all. Once the roughness reaches the height of the defect, the roughness then immediately moves into ②, where it remains exactly the same size as the defect.

The reason for the difference in behaviour of concave and convex defect profiles lies in the way the defects contribute to the overall roughness height. As the assumption for this simulation is that there will always be perfect chip removal, the roughness height R_t is determined by intersection of the tool profile (including the defect) with itself, horizontally off-set by the feed f. The convex defects contribute to the roughness height even at high feed rates, by adding a constant figure to the roughness height.

In comparison the concave defect actually reduces the roughness height slightly at higher feeds. As the defect removes part of the tool radius it effectively forms a secant through the tool profile, thus flattening the profile height slightly. The intersections of the tool profiles, which form the surface roughness, are hardly affected in height by the presence of the defect. With decreasing feed, the roughness height reduces just as quickly with a concave defect as it does with a defect-free cutting tool. Once the roughness height is equal to the defect height, the concave defect then becomes the determining factor for the roughness height. As long as the different sections of the tool profile do not cut into the ridges left by the concave defect, the roughness height R_t will remain constant.

Decreasing the feed rate further the simulated roughnesses depart from the plateau ② and decrease once more (③, ③a, ③b). Again the shape of the defect profile does not have a great effect, again the difference between concave and convex defects is more significant.

The decrease in surface roughness for convex profiles occurs once the feed rate f becomes smaller than the defect width ③. At this point the only relevant part of the cutting tool for the surface generation is the defect itself. In effect the cutting tool at this stage is a single point (in case of the triangular defect) or a small radius (in case of the circular defect) cutting tool. The roughness height is then only determined by the defect geometry and the feed. For a triangular defect the determining factor is the point angle of the profile. For circular defects the determining factor is the defect radius. It can be seen in the appropriate part of Figure 30 that the predicted roughness in ③ follows again the profile lines predicted with Equation 4 at their respective radii.

Concave defects show a different behaviour to convex defect profiles at low feeds. Here the departure from plateau ② occurs at higher feed rates than for convex profiles. The reason for this is that with decreasing feed the large radius of the tool profile starts to cut into the raised section of the surface left by the defect (③a). The point at which this happens depends both on the defect size and shape as well as the tool radius. Higher defect shapes and large tool radii both lead to the onset of this behaviour at larger feeds.

When the feed is decreased to the defect width and below, there is a small rise in surface roughness as the steeper flanks of the concave defects intersect with themselves. From this point onwards, the cutting tool then behaves like an asymmetric single point (or more correctly a two point) cutting tool (③b). The geometry of each point is partly made up from the large tool radius and partly from the flank of the defect profile, close to their intersection.

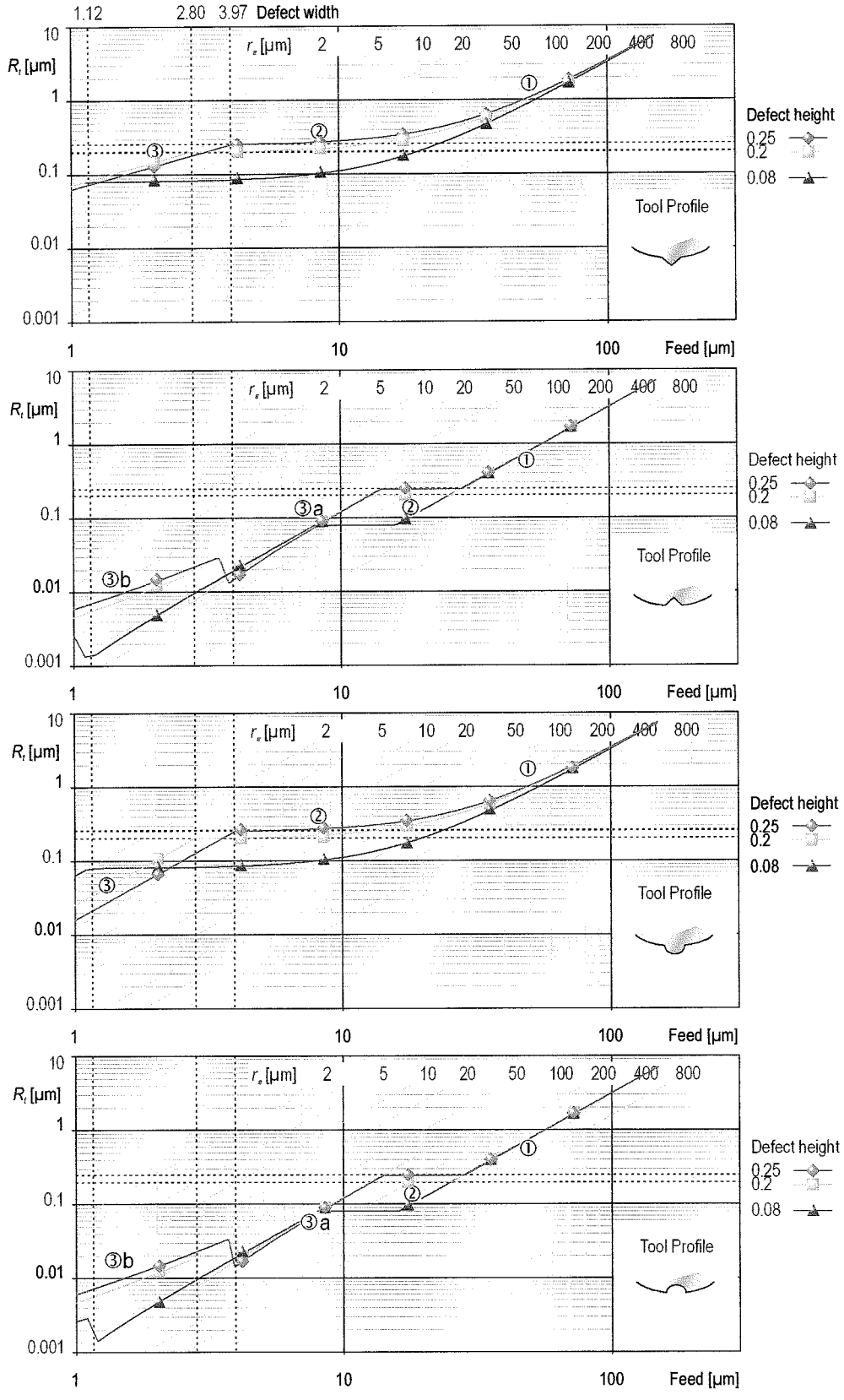

Figure 30: Roughness prediction (R_t) from cutting tools with single defects

5.2.2 Simulation of regular multi-defect cutting edges

In the previous chapter it was shown that the defect shape itself has only a small impact on the generated surface roughness. More important are the overall dimensions (height and width) and the orientation of the defect (convex or concave). In the light of this the simulation of regular multi-defect cutting edges was carried out with only sinusoidal defect shapes.

When assessing the impact of sinusoidal defects, not only are the height and width of the defect used of potential relevance but also the position of minima and maxima relative to the macro-geometry of the cutting tool. With sinusoidal defects this can be expressed as a phase shift of the curve relative to a datum position. In the following simulations the initial condition aligned the lowest point of the defect curve with the lowest point of the tool profile. The defect curve was subsequently phase shifted in constant intervals up to a total shift of 180°.

Figure 31 and Figure 32 show the outcome of simulations with constant tool corner radii and different defect sizes. The defects were phase shifted in 30° intervals for each simulation. Subsequently minimum, maximum and average values were calculated. Notable from both figures is that the phase shift has very little impact on the calculated surface roughness. The largest difference (in percentage terms) between minimum and maximum value can be seen Figure 31 at feed rates between 20 and 30µm. The variation however is only about half the height of the defect and significantly smaller than the variation seen in actual cutting tests (see Chapter 5.3.1).

Figure 31 shows the behaviour of a tool with a large defect. This tool behaves similarly to the cutting tools with a single edge defect examined above, where at high feed rates the tool behaves as if defect free. Decreasing feed rate leads to a section in the graph of constant surface roughness; further decreases in feed lead to a continuous drop in surface roughness down to single nanometre figures.

The behaviour of the cutting tool with small edge defects (Figure 32) is entirely different. Again the cutting tool behaves as if defect free at high feed rates. However reducing the feed leads to an oscillatory behaviour in the predicted roughnesses. The previously observed trend of stationary surface roughness and subsequent drop-offs in roughness with reducing feed still seems to be present. Superimposed on this are oscillations in surface roughness. The period of these (in feed) is equal to the defect width over the length of the graph, the amplitude is approximately half the defect height, but has a tendency to increase for lower feed values.

This behaviour is caused by the individual sinusoidal defects matching up from one work piece revolution to the next for feed rates which are multiples of the defect spacing. This effect produces rougher surfaces. The smoothest surfaces are produced if the defects are fully out of phase for subsequent work piece revolutions.

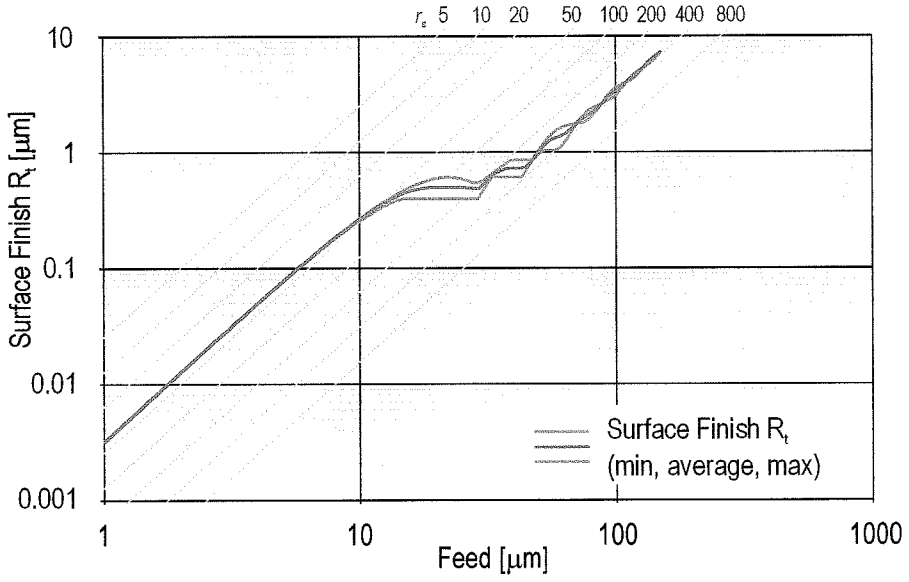

Figure 31: Surface roughness simulated with sinusoidal defects
(r_ε 0.4mm, defect height 0.47µm, defect width 19.8µm)

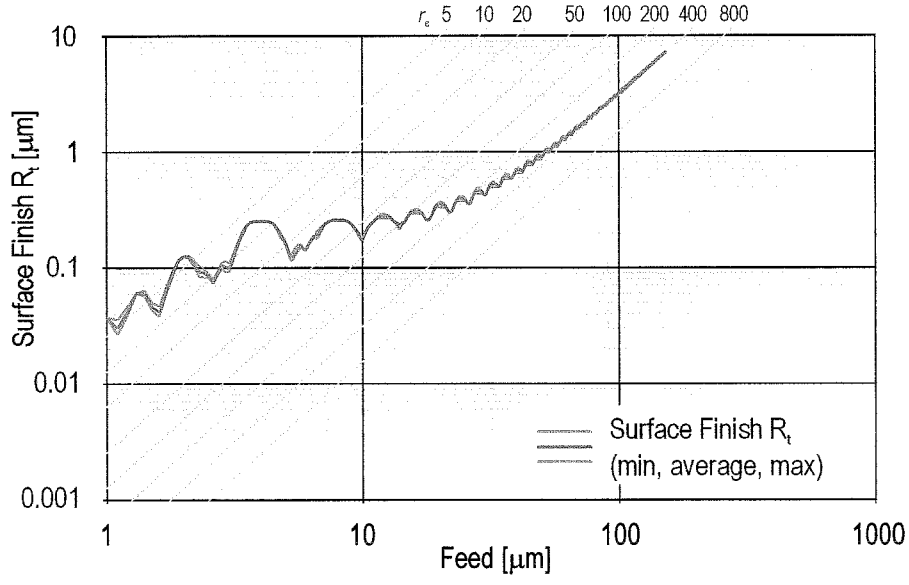

Figure 32: Surface roughness simulated with sinusoidal defects
(r_ε 0.4mm, defect height 0.25µm, defect width 3.97µm)

The simulated surface roughnesses all seem to follow the same basic underlying trend. The achievable roughness at a given feed rate is determined by the macroscopic tool geometry for high feeds and by the size and shape of the defects in the cutting edge for lower feeds. The defect profile as such seems to play only a minor role. Important however are defect height and width and – for single defects – the orientation of the defect (convex/concave).

The common underlying trend is such that at high feed rates the cutting tools behave as if defect-free. Reducing feed leads to decreasing surface roughness until the roughness approaches the defect height. At this stage the surface roughness stabilises until the feed becomes smaller than the defect width. Further reductions in feed lead to a continuous decrease in roughness. This behaviour is illustrated in Figure 33.

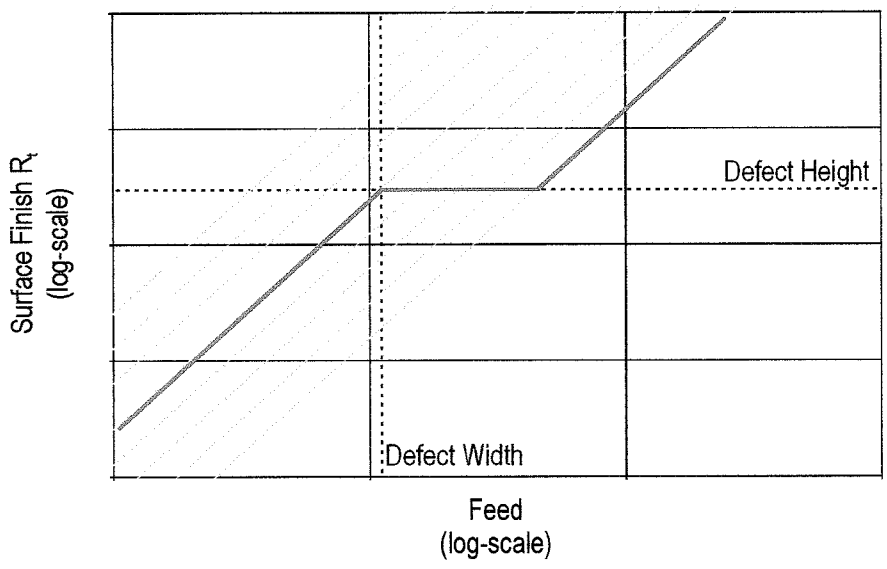

Figure 33: Underlying trend in dependency between feed and surface roughness (R_t)

5.3 Cutting tests with standard cutting tools

Cutting tests were carried out with standard cutting tools on work pieces as described in Chapter 2.1.5. Tools were used for three cuts of 50m length each, then replaced. This was done to eliminate the effect of tool wear at this stage. For each CBN grade eight different feed rates were tested ranging from 150µm down to 1µm.

5.3.1 Surface roughness from short assessment lengths

Figure 34 shows the experimentally achieved roughnesses (R_t) averaged from three cutting trials. All cutting tools had a nominal corner radius of $r_\varepsilon = 0.4$ mm. Surfaces were measured on the Form Talysurf, the primary data was exported and assessed with specially developed software tools. Initially surface roughness assessment was based on short assessment lengths of 10×feed. This was deliberately done to eliminate any relative error motion between tool and work piece and to isolate cusp height and shape for evaluation. The averaged results (R_t) are shown in Figure 34.

At the highest feed rate (150µm) results are clustered together quite closely, but all are better than expected from a 0.4mm tool. While some of this effect may be due to deviations of the actual tool radius from the nominal size, it is more likely that rounding at the tip of the surface cusps reduces the overall roughness.

Reducing the feed to 80µm or below leads to a considerable spread of results. For all these feed rates the ratio between lowest and highest achieved roughness is a factor of 5× or more. This clearly indicates the differing performance of the various CBN grades.

The overall trend seen in the surface roughness simulation is reflected in the results. Reducing the feed from 150µm leads to a drop in surface roughness. In the medium feed range (ca. f=80 down to f=5µm) the roughness decreases more slowly or even levels, while at very low feeds (f=1 and f=2µm) the decrease in surface roughness accelerates again.

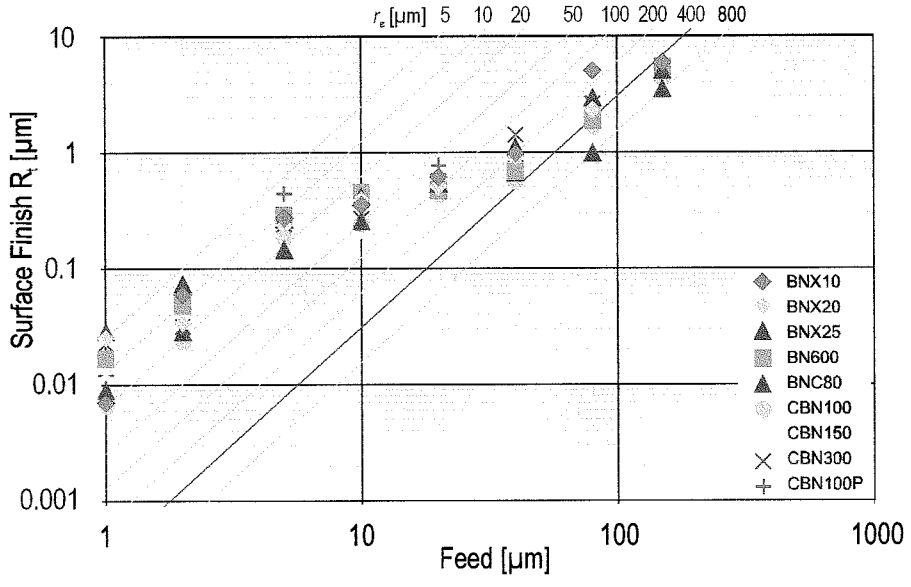

Figure 34: Roughness R_t vs. Feed (averaged from three cutting tests)

The CBN grades which achieved the lowest roughnesses are BNX10, CBN100 and BNC80 (at f=1µm). It was possible to obtain roughnesses of R_t<0.01µm. All other grades achieved roughnesses of R_t>0.01µm, some as much as R_t=0.03µm.

5.3.2 Cutting edge quality

Considering the effect of cutting edge defects on the simulated results an assessment of cutting edge quality was carried out. Over an area 0.1mm wide surface roughness parameters R_a, R_t and S_m were determined. This was done by examining the imprints of new cutting tools on short lengths of machined surfaces. These were obtained at high feed rates of f=0.2mm. Note that in [21] it was found that there is very good agreement between actual edge profile and surface topography on hard turned surfaces. This effect is exploited here in the measurement of the cutting tool profile in the tool reference plane.

A summary of these results is given in Table 8. Considering the range of CBN grain sizes in the different grades results do not show much spread. Typical surface roughnesses are R_t=0.34µm and S_m=10.2µm (excluding the BNX25, Genta Coating). There seems to be no statistically significant correlation between CBN grain size and any of the surface roughness parameters. While this is unexpected it may be that at the early stage in the tool life, when all the figures below were recorded, the manufacturing process rather than the grain size determines the edge quality.

One effect is noticeable however: Coatings seem to have a detrimental effect on edge quality. Both the coated BNX25 and the CBN100 perform worse in terms of edge roughness than the uncoated grades. BNC80, which is also a coated grade, performs about average.

The reason for the detrimental effect of the coatings is probably the fact that on occasion all coatings were seen to chip off their CBN substrate. While this only happened to a lesser degree with the coatings applied by the cutting tool manufacturers (BNC80 and CBN100p), the tested third party coating exhibited severe failure even after very short lengths of cut. Figure 35 shows a micrograph of one of those cutting tools. On the tool face one large chipped area is visible, while on the flank at least three different defect lines can be identified (see arrows), where individual layers of the coating have become detached. Nevertheless chipping of the coating could at least be seen occasionally on all tested coated CBN grades.

Grade	Average R_a	Average R_t	Average S_m
BNX10	0.06µm	0.34µm	11.02µm
BNX20	0.05µm	0.31µm	10.15µm
BNX25	0.05µm	0.36µm	9.52µm
BNX25, Genta Coating	0.25µm	1.81µm	19.01µm
BN600	0.07µm	0.47µm	9.40µm
BNC80	0.05µm	0.38µm	9.53µm
CBN100	0.03µm	0.17µm	8.36µm
CBN100P	0.06µm	0.37µm	10.57µm
CBN150	0.02µm	0.14µm	9.62µm
CBN300	0.08µm	0.50µm	12.76µm
Average (excl. Genta Coating)	*0.051µm*	*0.334µm*	*10.103µm*

Table 8: Cutting Edge Roughness Parameters

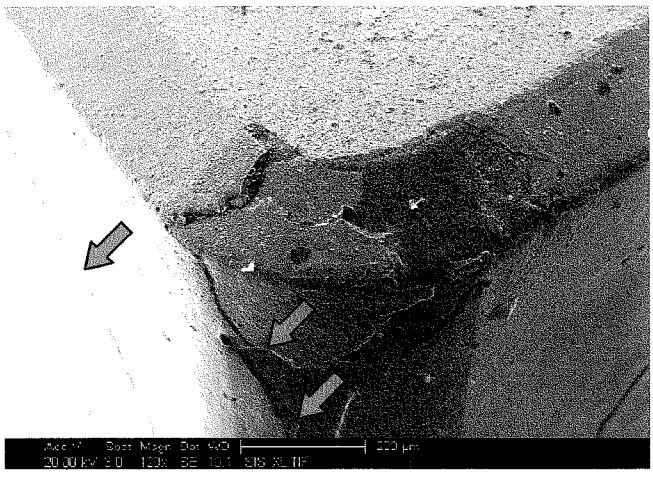

Figure 35: Scanning electron micrograph of severe coating failure

In addition to the defects along the cutting edge, data was supplied by one cutting tool manufacturer for edge quality measured in the tool back plane (Figure 36, Table 9). Figure 36 illustrates the measurement of the cutting edge radii. A circle is fitted to the measured cutting tool profile (green line). The radius of this circle is taken as the edge radius. A measurement of how well the cutting edge matches a circle is given by the offset distance. This distance was typically 2-4µm in the supplied data. Cutting edge radii for eight tools from grades CBN100, CBN100P, CBN150 and CBN300 are given in Table 9.

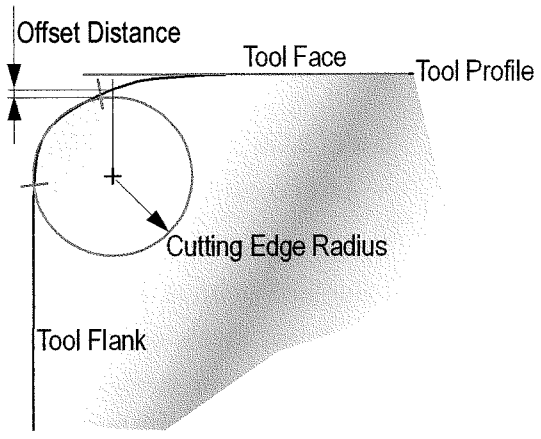

Figure 36: Measurement of the Cutting Edge Radius

Grade	Tool 1	Tool 2	Tool 3	Tool 4	Tool 5	Tool 6	Tool 7	Tool 8	Average Radius	Standard Deviation
CBN100	9µm	13µm	10µm	11µm	12µm	7µm	9µm	11µm	10.2µm	1.9µm
CBN100P	18µm	14µm	14µm	14µm	12µm	11µm	12µm	15µm	16.8µm	2.2µm
CBN150	11µm	9µm	10µm	8µm	8µm	8µm	22µm	28µm	13.0µm	7.7µm
CBN300	18µm	29µm	27µm	24µm	23µm	10µm	16µm	19µm	20.5µm	6.2µm

Table 9: Cutting Edge Radii measurements (supplied by Seco Tools UK)

In the data recorded in the tool reference plane it was not possible to see a correlation between CBN grain size and defect size; this is different when it comes to the cutting edge radius. Looking at the average radii it is clear that the grades with the small CBN sizes (CBN100, CBN150) yield smaller edge radii, while the larger grain size CBN300 has a significantly larger radius. Also, adding a coating to CBN100 increases the edge radius (CBN100P), which is to be expected.

While results for CBN100 and CBN100P show very little variation, the other two grades exhibit much higher standard deviations. CBN300 just seems to give varying results, whereas the CBN150 tools are different. Tools 1 to 6 came from one batch and have very little variation (σ=1.3µm). Tools 7 and 8 were supplied sometime later from a different batch and lead to the high standard deviation seen in Table 9.

There are indications that the cutting edge radius has a strong impact on the stability of the cut at low feed rates. The number of edges with large cutting edge radii at low feed rates is still too small to come to a final conclusion. However those tools which were observed to chatter at feeds f=1-2µm all had cutting edge radii of around 20µm or more.

5.3.3 Surface roughness from long assessment lengths - Influence of asynchronous error motion

When the same surfaces which were evaluated in the previous section are examined with a longer assessment length a clear difference in surface roughness levels can be seen. Figure 37 gives an example of this behaviour based on work pieces machined with CBN100 grade tools. At high feed rates (f=40 to 150µm) there is little difference between roughnesses measured from short assessment lengths (10×f) and long assessment lengths (50-100×f). With reducing feed the two curves diverge, with the short assessment length always giving the lower roughness. The divergence goes so far that at f=1µm there is approximately an order of magnitude difference in roughnesses measured at different assessment lengths.

The reason for this becomes clear on closer examination of the surface roughness traces. While the cusp height remains reasonably stable over a given trace, the position of subsequent feed marks on the work piece shifts in a direction normal to the feed direction (see Figure 38). This represents an error motion of the cutting tool relative to the work piece surface and can contribute significantly to the surface roughness. In order for the error motion to have an effect of the surface roughness it has to be asynchronous with respect to the spindle rotation. There are likely to be more factors involved than just the asynchronous spindle error motions measured with a capacitance gauge against a precision ball (as described in [60]).

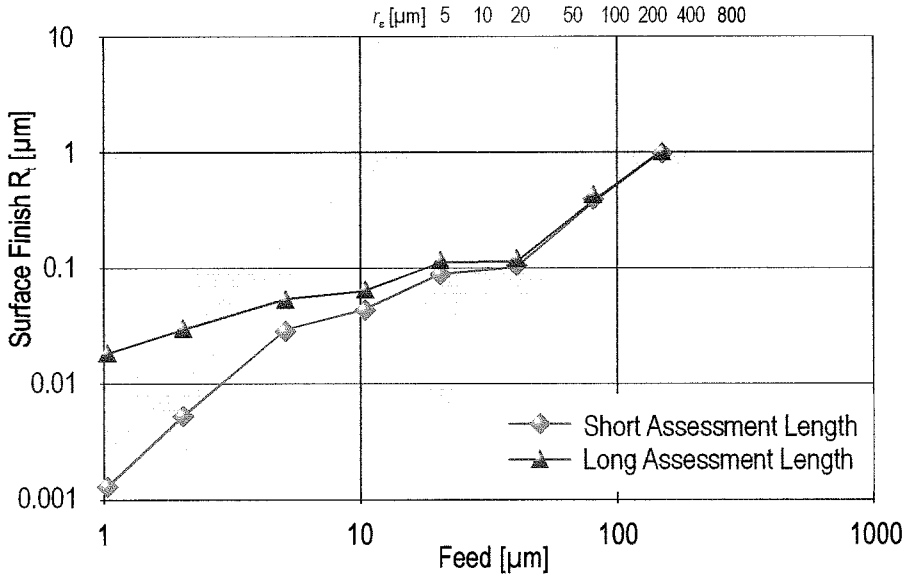

Figure 37: Difference in surface roughness due to change in assessment length (machined with CBN100)

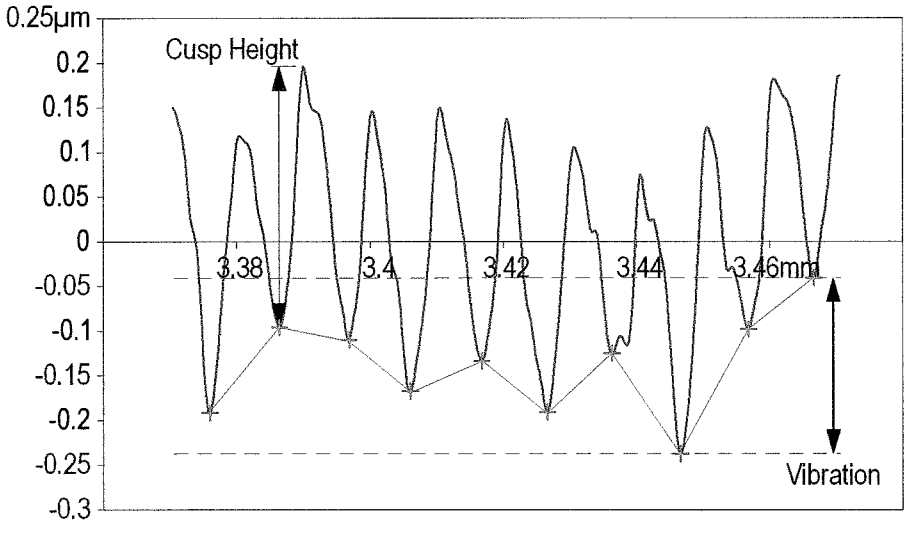

Figure 38: Vibration contribution to surface roughness

The relevant vibration is added up from all sources of vibration in the machine including:

- Spindle asynchronous error (axial, radial and tilt)
- Machine servo/axes instability
- Hydraulic vibration (in hydrostatic slides and spindles)
- Resonances of the machine of machine elements, in particular tool holder and work holding

Inconsistencies in the work piece material (e.g. hard inclusions) can also contribute to the observed error motion even by offering different resistance to the cutting tool from one work piece revolution to the next.

The level of vibration is also influenced by the cutting conditions. The feed rate and selection of cutting tool can have a big impact on the level of vibration (see Figure 39). The graphs for CBN100 and BNX10 have been selected as representative for most of the tested CBN grades. These show a steady decrease in vibration as feed rate is reduced. Ultimately the vibration levels off at a magnitude which is very similar to the asynchronous spindle error measured, in compliance with [60], [35].

CBN150 has been selected as representative for a second group of cutting tools, which show a marked increase in vibration at low feed rates. This is not necessarily an effect of the particular CBN grade, it is more likely that the large cutting edge radius common to these tools caused the increase in vibration. Vibration at this level is commonly referred to as tool chatter.

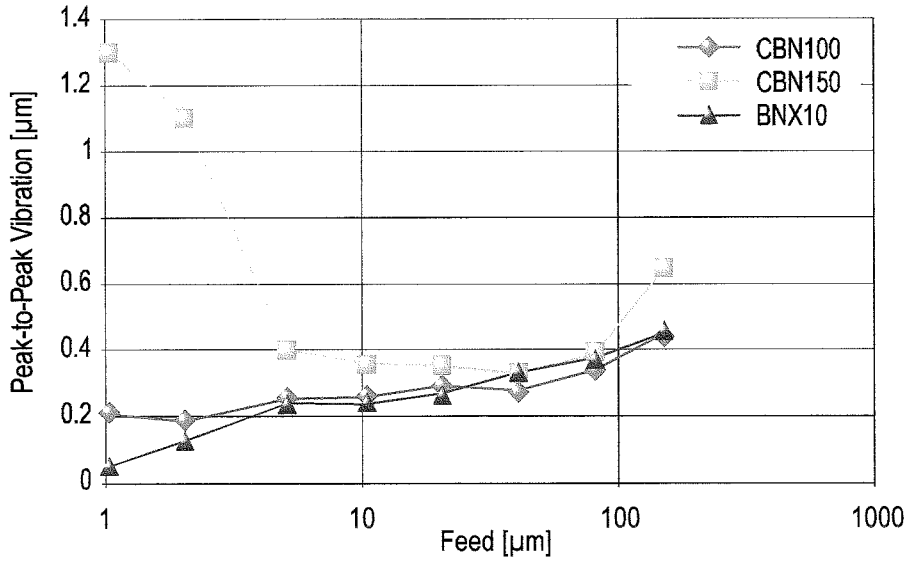

Figure 39: Peak-to-Peak vibration levels

The difference in vibration between the different cutting tools is illustrated in Figure 40. The asynchronous error motions are shown over a length of 1mm on the work piece machined at f=1µm. Two key differences between the graphs are immediately visible: The magnitude of vibration is much smaller on CBN100 and BNX10 than it is on CBN150. Also BNX10 and CBN100 seem to cause vibration dominated by higher frequencies, whereas CBN150 causes mainly lower frequency vibration.

It must be remembered that the frequencies examined here are spatial frequencies recorded along the feed direction of the cutting tool. This records the relative cutting tool position once per revolution of the work piece. The absolute frequency or frequency spectrum of the asynchronous error cannot be recorded reliably in this way. This would require a greatly increased sampling rate around the circumference of the work piece. While this is a limitation in this particular sampling technique, it does give useful results for analysing surface roughness.

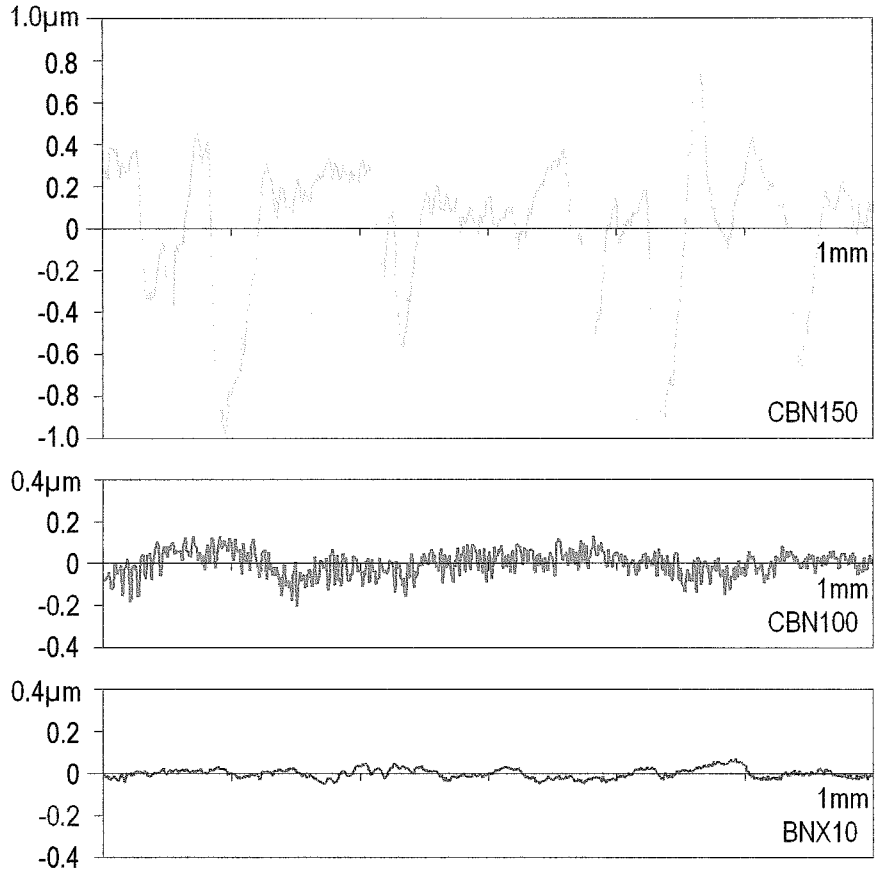

Figure 40: Asynchronous Error Motion at f=1µm measured off surface roughness

5.4 Refined simulation of surface roughness generation

In the light of the effects the asynchronous error motion has on the surface roughness it was necessary to adjust the surface roughness simulation developed earlier. The updated flow diagram is shown in Figure 41. Added to the previous version is the input for the error motion. This is done by specifying the standard deviation of the error motion. This value is subsequently used to apply a random, normally distributed offset to the tool position prior to the calculation of the chip profile. The remaining simulation software remains unchanged.

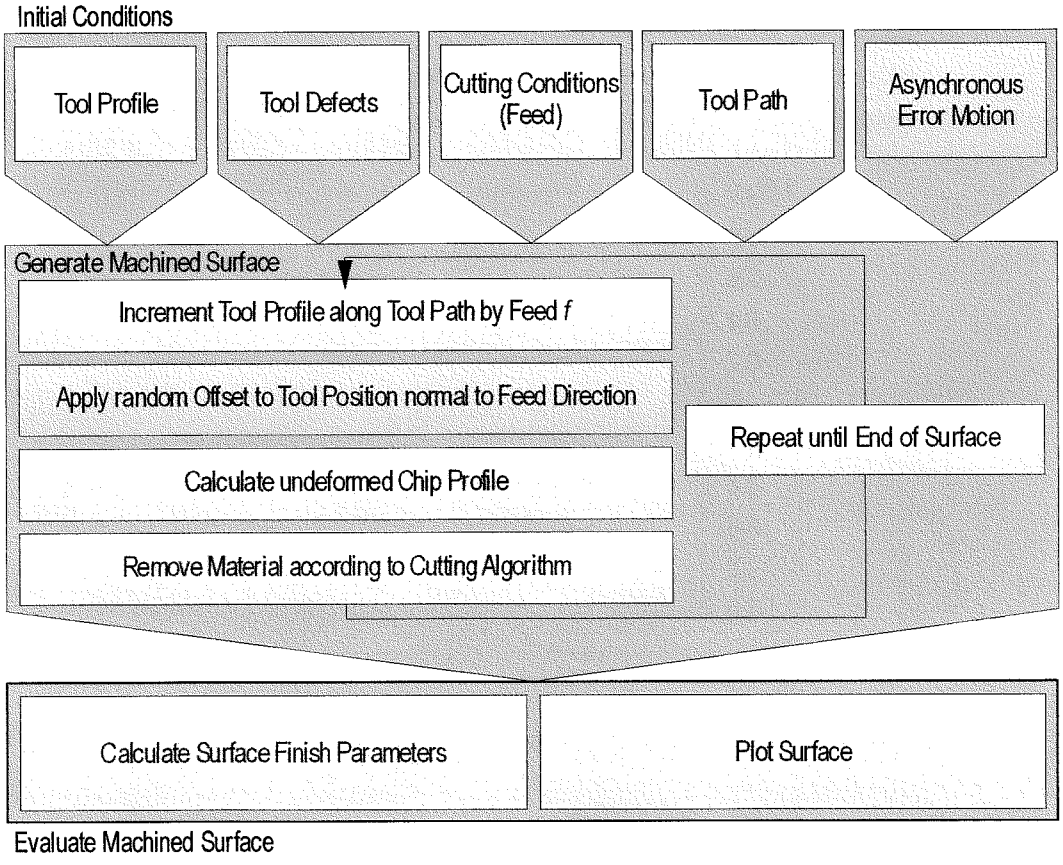

Figure 41: Flow diagram of surface roughness simulation including synchronous error

Calculating surface roughnesses from a range of asynchronous vibration levels leads to a group of graphs as shown in Figure 42. The dashed line in Figure 42 is given for reference and shows the simulated performance of a cutting tool with a defect height of 0.33µm and a defect width of 10.1µm without any error motion. With increasing vibration levels the graphs diverge from the reference line. The divergence initially happens at low feed rates (see σ=0.01µm curve) and a close similarity with the reference line can be maintained for feeds rates of f>8µm. This only changes in the curve with σ=0.3µm, where the divergence from the reference line happens at approximately f=70µm. Note that with this curve the total level of ca. 3×σ is considerably larger than the simulated defect height.

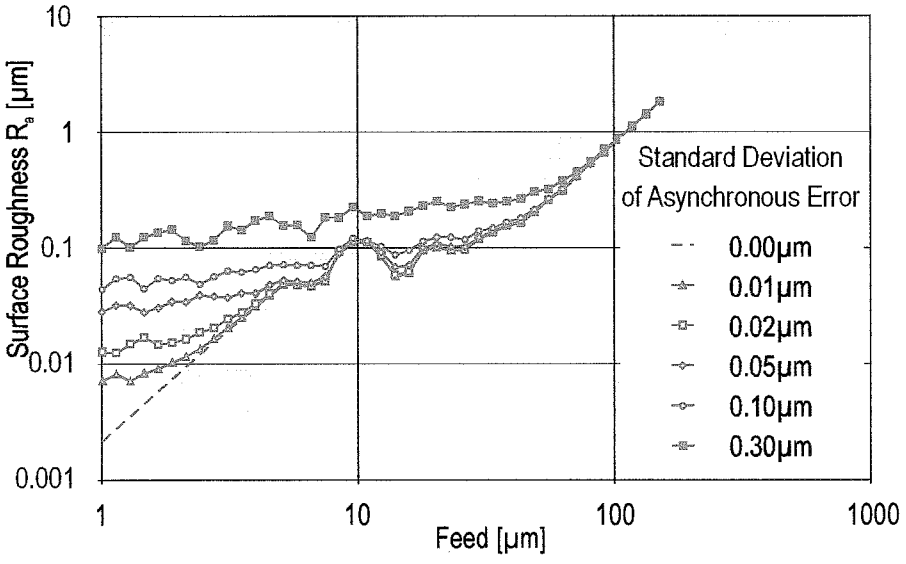

Figure 42: Effect of different vibration levels on surface roughness R_a (Tool Defect Height: 0.33µm, Defect Width: 10.1µm)

Figure 43 shows the level of agreement that can be achieved between measured roughnesses from cutting trials and simulated roughnesses. The defect height and width remain unchanged from the previous simulation at 0.33µm and 10.1µm respectively. The vibration level has been set to σ=0.07µm for all simulated roughnesses. For both R_a and R_t very good agreement has been reached between simulation and experiments.

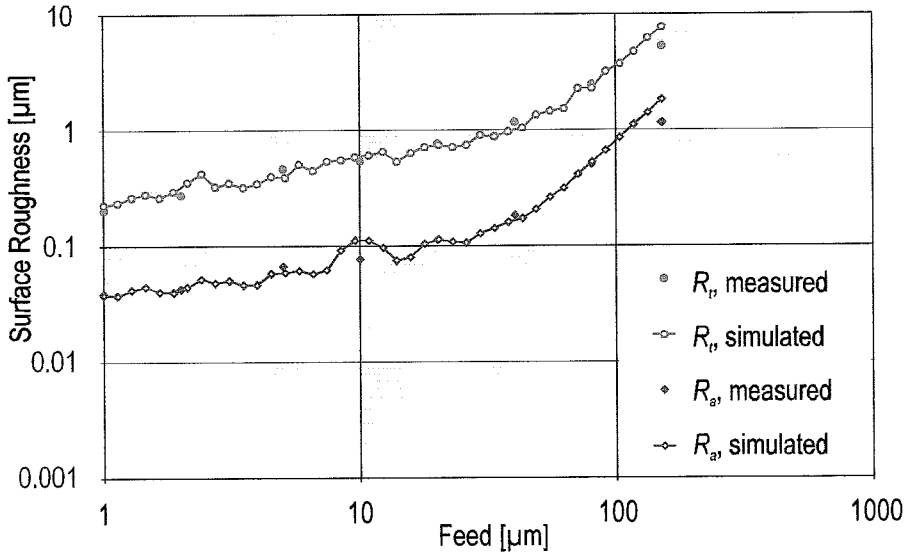

Figure 43: Comparison between measured and simulated surface roughnesses (R_a, R_t)

From the work described in previous sections one can summarise that to predict the surface roughness in hard turning the following properties need to be known:

- Tool corner radius
- Tool defect height
- Tool defect width
- Feed
- Asynchronous vibration level

With this data it is possible to predict the surface roughness with a very good degree of accuracy for a wide range of feed rates. Note that this model will not work when machining porous material or material with hard inclusions, which lead to incomplete chip removal or break-out. Also not taken into account is the phenomenon of chip side flow.

Despite the fact that these limitations exist the hard turning process is surprisingly deterministic. If the tool defect shape and the level of vibration is known, the surface profile and the derived roughnesses can be calculated very accurately. Variation in achieved surface roughness can be explained with changes in one of the input variables. In this light the hard turning process follows Bryan's 'Determinism' as well as Loxham's or Portas's principle [61].

While the modelling of hard turning can be used whenever a suitable computer is available, it may be more practical to have something that can be used under workshop conditions without explicitly knowing all the above inputs. In particular the tool defects and the vibration level may not be readily available to machine operators. To simplify the selection of cutting parameters at the shop floor level it is possible to create roughness 'fingerprints' for a given machine/cutting tool combination. These fingerprints show the expected range of surface roughnesses from a given cutting tool for its usable range of feed rates. With a sufficiently large data set the fingerprints could be calculated for a desired confidence level (e.g. 95% or 99%) and used as a method for improving and maintaining product quality.

Some preliminary fingerprints are shown in Figure 44 (grey shaded areas). They are preliminary as they are based on a fairly small set of data for each CBN grade and have been calculated from maximum and minimum recorded values rather than from standard deviations. Despite this they envelop most of the roughnesses from the experiments (red dots). It also shows one of the potential pit falls: If tool chatter develops (see CBN150 and CBN300) the actual surface roughnesses are far worse than predicted by the fingerprint. Nevertheless these fingerprints are a useful look-up device for selecting the right CBN grade and feed rate for a desired surface roughness.

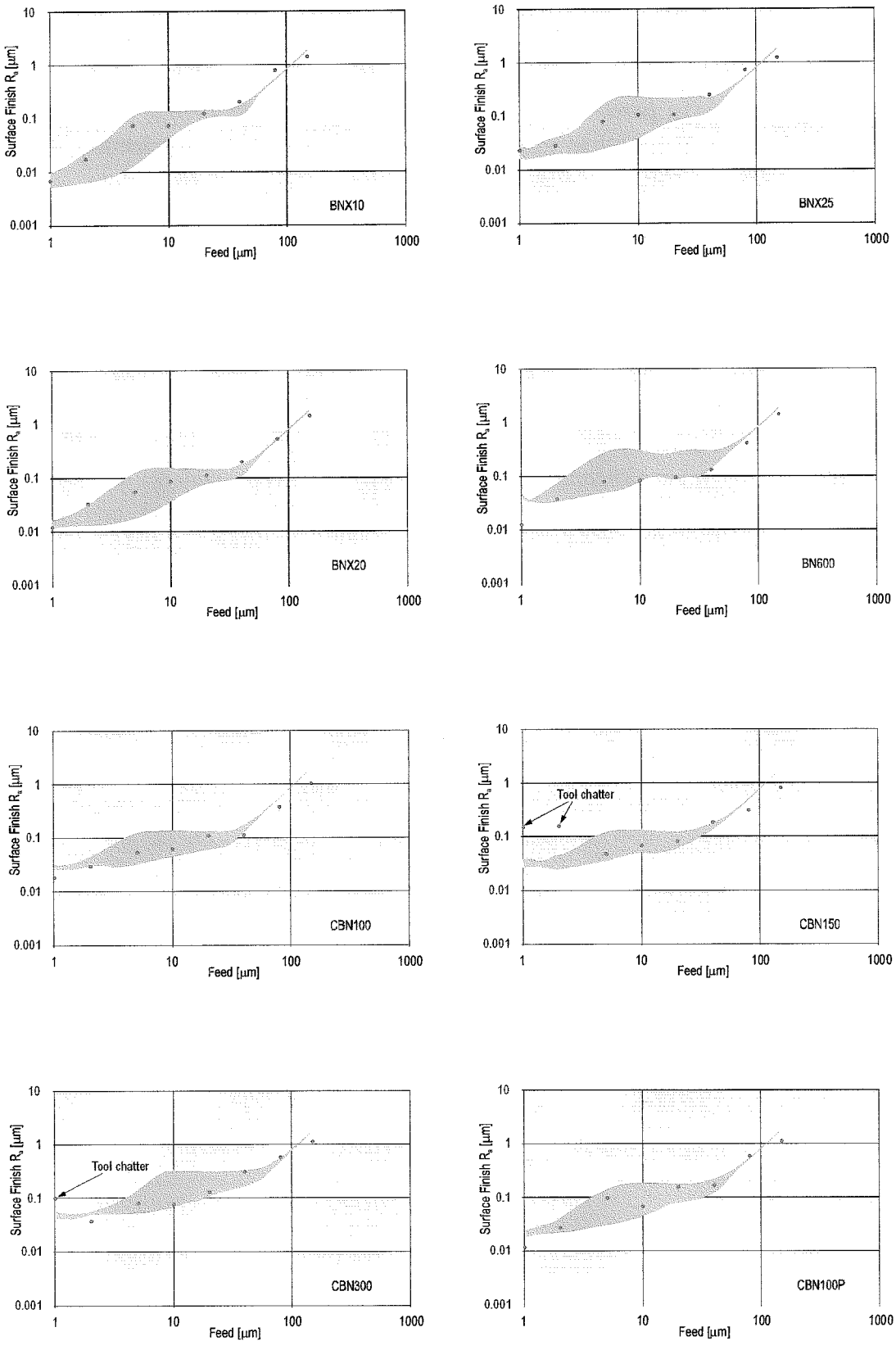

Figure 44: Machine/Cutting tool fingerprints (grey areas) and experimental results (red dots)

Using the data recorded in the cutting tests and applying it selectively in the roughness simulation it is possible to separate the relative effects that tool (macro) geometry, tool defects and machine vibration have had on surface roughness with varying feed rates (Figure 45).

At high feed rates (f>80µm), the tool geometry completely dominates in generating surface roughness. From f=40µm down to f=10µm the tool defects become of increasing importance, causing almost all the surface roughness at f=10µm. Machine vibration is negligible in this feed range.

Vibration only becomes relevant at f=5µm and below, contributing approximately 20% of the total roughness at f=5µm and 70% for feed rates f=2µm and f=1µm.

These proportional effects are typical for the particular conditions these experiments were conducted under. The contributions will shift if significantly different input values are chosen. So if – for example – a machine tool with much higher vibration levels was used, then the vibration would have a stronger effect at higher feed rates.

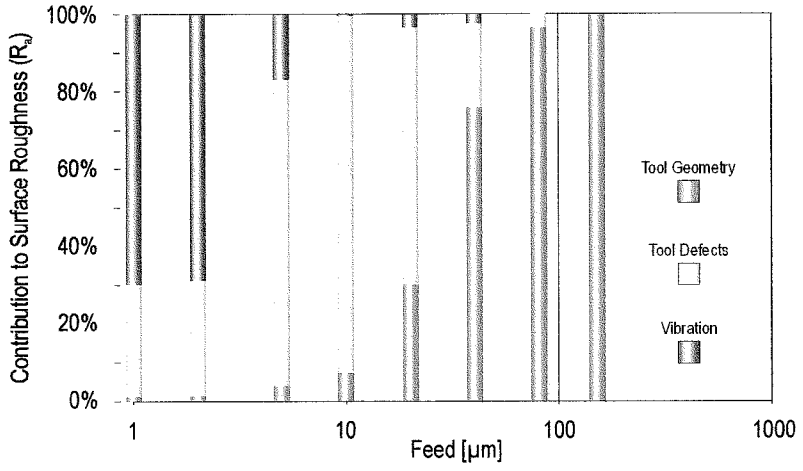

Figure 45: Causes and their relative effects on surface roughness (new tools, r_ε0.4)

Nevertheless this diagram shows clearly the importance of controlling tool defects. Hard turning feed rates rarely drop below f=5µm even in super-precision applications for reasons of productivity. So machine tool vibration can largely be ignored, if kept within reasonable levels. The tool geometry of course is actively chosen by the machine operator to suit a particular work piece geometry.

However tool defect size is something largely absent from CBN tool manufacturers' brochures and published specifications. Manufacturers of high-precision diamond tools offer tools with 'controlled waviness' and it would be highly desirable from a user's point of view to have something similar for high- and ultra-precision hard turning. It is understood that due to the polycrystalline nature of CBN it is unlikely that the same levels of waviness, roughness and sharpness will be achieved with CBN than with monocrystalline diamond. Still a specification for cutting edge roughness (both in terms of defect height and width) would be useful data for optimising the hard turning process.

5.4.1 Tool 'fingerprints' in the assessment of tools with wiper geometry

One of the developments in cutting tools that is advertised to deliver a significant improvement in surface roughness is the use of so called "wiper tools" . Wiper tools are designed to have a small clearance angle between the machined work piece surface and the minor edge of the cutting tool. The dimensions for the wiper tools used during this work are given in Figure 46. This is a relatively simple tool with a straight wiper edge of approximately 1mm in length and with a nominal clearance angle of 0.5°. Tool manufacturers and researchers alike are developing more complex wiper geometries with a series of one or more blended radii to optimise performance.

One of the main practical difficulties in using wiper tools is the setting of the small clearance angle. Many tool holding systems suffer from a certain lack of repeatability due to the a build up of tolerances, in particular in those cases where a tool shank is clamped in a separate tool holder. In conventional turning applications this is not a particular problem as common tool setting procedures overcome the axial and radial errors that are introduced. This is not the case for angular errors though and readings taken with an optical tool pre-setter indicate that the clearance angle can vary by ±0.2° or more. The clearance angle however has a large impact on the generated roughness and the stability of the cut. Very small positive or even negative clearance angles do not allow stable cutting as the interference between wiper and work piece becomes too large.

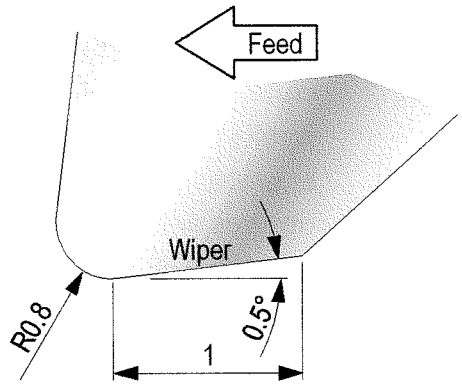

Figure 46: Wiper tool geometry used in cutting trials

Results from fingerprint simulation for a wiper tool in comparison to a standard cutting tool and experimental results are shown in Figure 47. The tool fingerprints show clearly that the wiper tool gives much lower surface roughness than the round-nose cutting tool at high feed rates. The wiper tool also remains usable for much higher feed rates than the round-nose tool. There is little point in using a conventional tool for feed rates that are larger than the nose radius as surface roughness rises excessively. In fact depending on the depth of cut the tool may only cut a spiral groove into the work piece rather than generating a new surface. This is not so with the wiper tool. In theory the wiper tool can be used for feed rates that are at least equal to the wiper length without that same deterioration of surface roughness. It is still true that high feeds will lead to rougher surfaces with a wiper, but not to the same extent as with a round-nose tool.

The wiper fingerprint shows a levelling of surface roughness at a feed rate of below approximately f=100µm and at a roughness of R_a≈0.1µm. This levelling is due to the effect of the cutting edge roughness described previously and can also be observed for the round-nose tool at around f=40µm. Below the point where both cutting tools' roughnesses level off the surface roughnesses generated are in fact quite similar. For the medium feed range (f=10-100µm) the wiper tool exhibits a wider spread of roughnesses than the round-nose tool, but the predicted maximum roughnesses are very similar for both tools. Below f=10µm there is little difference between the two tools.

When comparing the predicted fingerprint of the wiper tool with the corresponding experimental data it becomes evident that the experimental results at f=100µm are somewhat better than the roughness prediction. This is probably due to the angular tool setting errors described above. For the other experimental feed rates of f=50µm and f=5µm there is good agreement between simulated and experimental results.

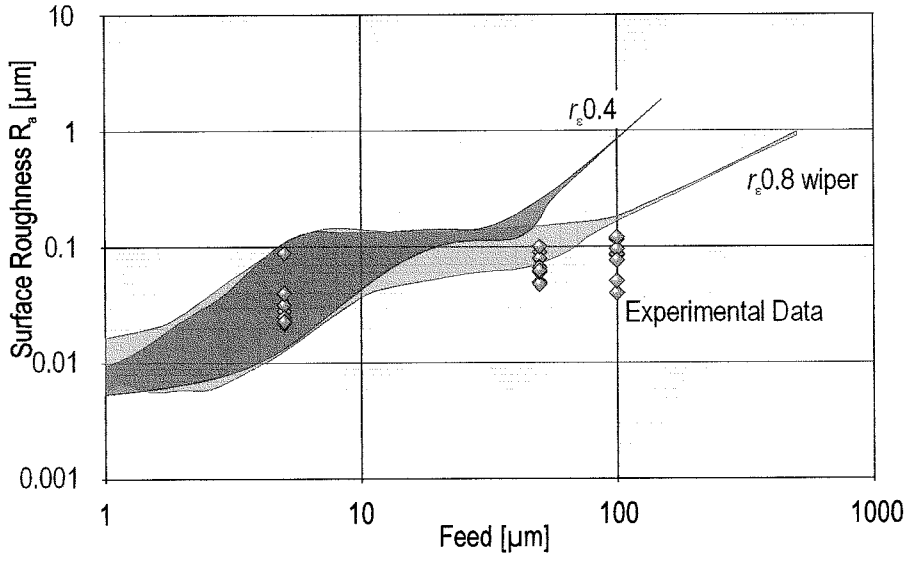

Figure 47: Fingerprints for round nose (r_ε 0.4) and wiper tool (r_ε 0.8, 0.5° wiper)

From these observations it is evident that wiper tools offer very large potential benefits at high feed rates. If the tool setting issues are overcome wiper tools allow increases in feed of up to 200% in comparison to the round-nose tools possibly even more, while maintaining the same surface roughness. At low feed rates however wiper tools do not offer a significant advantage over conventional tool geometries as the effect of machine vibration and cutting edge defects dominate surface roughness generation. It is unlikely that different wiper tool geometries will improve surface roughness at low feed rates unless improvements in cutting edge quality are made at the same time.

5.5 Tool wear at low feed rates

Tool wear in hard turning is normally associated with the formation of a notch on the trailing edge of the cutting tool and a more uniform material loss along the rest of the cutting edge (see Section 2.1.5.1) leading to a wear mark on the tool flank. It is known that this leads to a degradation of surface roughness over the tool life. In the following section the important manifestations of wear in low feed hard turning are examined for their influence on the achievable surface roughness.

5.5.1 Flank wear

The commonly used measure for tool wear in hard turning is the wear mark width V_B (see Figure 9). Plotting the measured wear mark width versus the cutting time t_c (Figure 49) it is apparent that within the first five minutes of cutting a wear flat between 40 and 50µm is established for feed rates between f=2-40µm. Only for f=150µm the wear flat is smaller (ca. 20µm). After t_c=5min the progression on the wear mark width tends to slow down or even stagnate at times until V_B=60-80µm is reached after t_c=20min. As a tendency the wear mark is wider for smaller feed rates than for higher feeds after the same cutting time (Figure 48).

Note that the wear mark widths reached after t_c=20min would still allow machining to continue without any adverse effects on the surface integrity of the work piece. As suggested in [3] hard turning tools can be used up to V_B=150µm before significant changes in surface integrity can be seen.

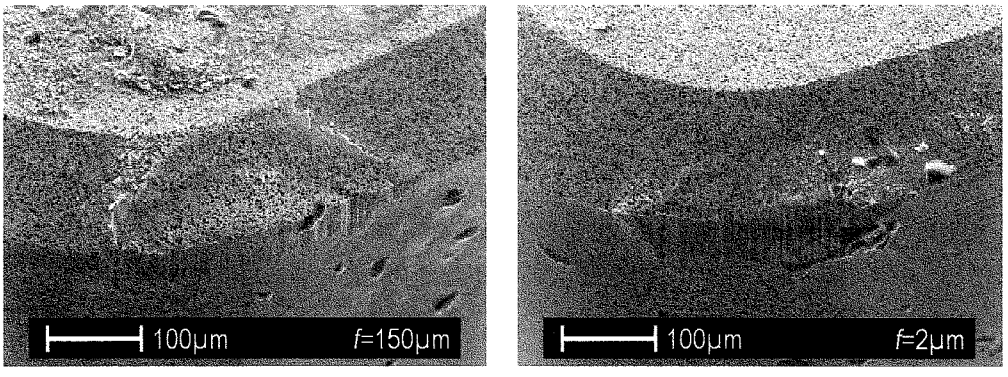

Figure 48: Wear marks on tools after t_c=20min

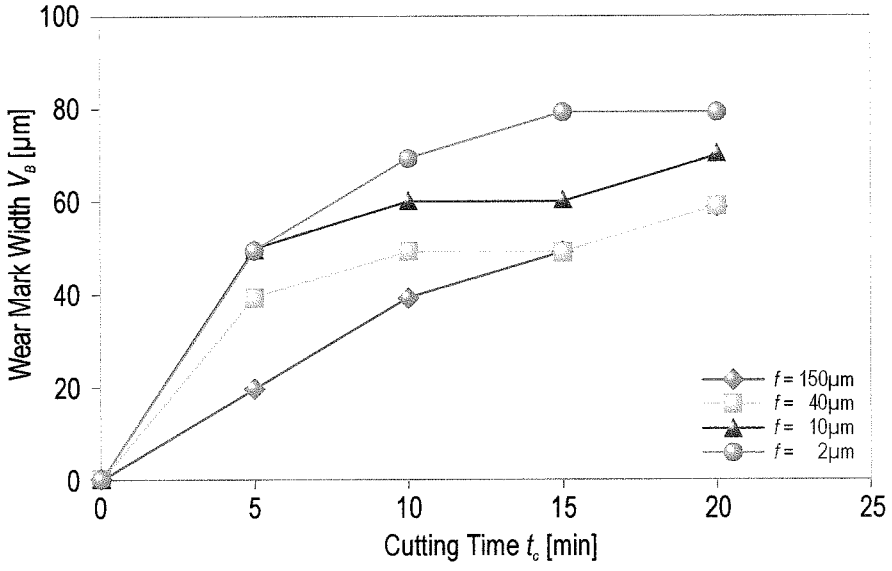

Figure 49: Wear mark width development with cutting time

5.5.2 Notch wear

In hard turning with low feed rates flank wear and notching have been observed. Keeping in mind the importance of the size of cutting edge defects on the achievable surface roughness the notch formation is of crucial importance for ultra-precision hard turning.

At the highest feed rate (f=150µm) the notch appears on the minor cutting edge (see Figure 50), while wear on the major cutting edge is quite small. As the feed rate is reduced to f=40µm the notch moves forward along the profile and eventually onto the major cutting edge. Once a notch has moved past the centre of the cutting tool a further notch appears on the minor cutting edge with the notch spacing equal to the feed rate.

At a feed rate of f=10µm the notches have moved some way up the major cutting edge (see arrows) and at least seven individual notches are visible. The spacing of the notches has decreased with the feed rate, the notch depth has also decreased.

When reducing the feed rate further down to f=2µm something seemingly surprising happens – no notching takes place. The only visible wear is an overall retraction of the lowest part of the cutting edge and of the major cutting edge.

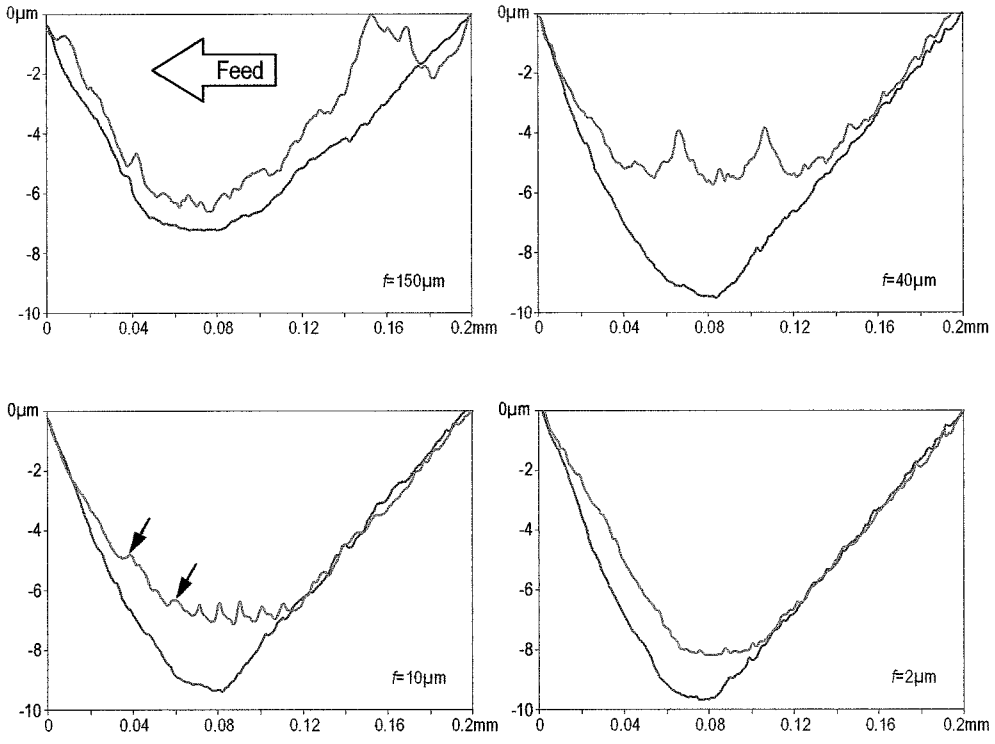

Figure 50: Comparison of new and worn cutting tools after a cutting time t_c=20min

Having been critical of Brammerz's formula for predicting hard turned surface roughnesses in Section 5.1 it has to be pointed out here that the development of wear notches is consistent with his work on the effect of a minimum undeformed chip thickness. So despite the fact that Brammerz's formula does not apply to hard turning with new tools his fundamental theory does have some bearing on hard turning.

Notch wear in hard turning starts in the precise location of the chip root and gradually moves upwards and forwards as the cutting tool wears. This behaviour can be seen in Figure 52 and has been reproduced in an adapted surface roughness simulation, which takes account of notch wear, but ignores all other kinds of wear (Figure 51). Note that the algorithm used in the simulation can predict the location of the notch, but is unsuitable for accurately determining notch height at a given time. In both measurement and simulation the initial notch grows until it is large enough and in the right position so that its imprint on the work piece surface intersects with the secondary cutting edge. Once this occurs the formation of a second notch can be seen on the cutting tool, with distance feed f behind the first notch (time '$8 \times t$' in Figure 51, time 4min in Figure 52).

The same behaviour causes the large number of notches observed at f=10µm.

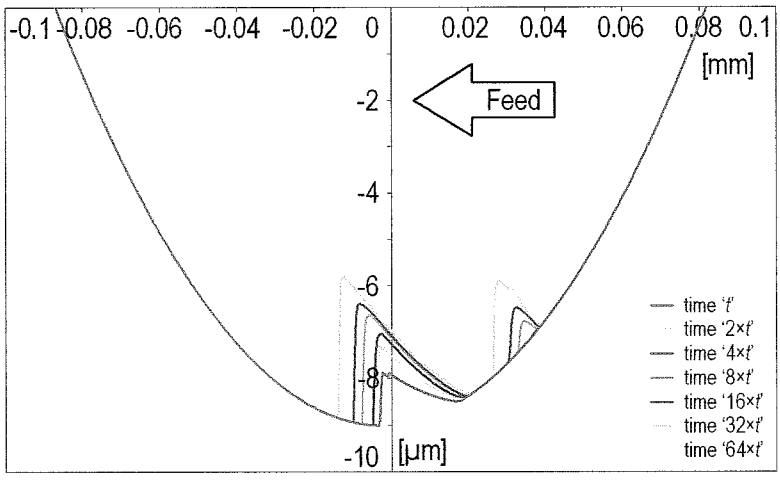

Figure 51: Simulation of Notch Wear Propagation at f=40µm

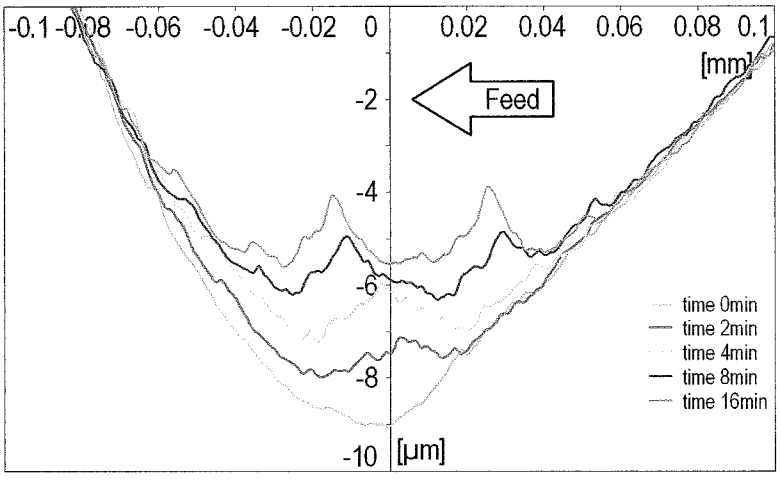

Figure 52: Measured Notch Wear Propagation at f=40µm

The interesting question is – why are there no notches visible at f=2µm? To answer this question it is necessary to examine the size of the minimum undeformed chip thickness h_{min} in relation to the feed. Going back to Equation 7 for a cutting edge radius r_n=20µm one obtains h_{min}≈1.9µm. Clearly there is little difference between feed and minimum undeformed chip thickness. As a consequence the notch position moves so far forward on the cutting edge that it never appears as a notch on that part of the cutting edge which generates the final work piece surface. Figure 53 shows the simulated notch wear effect on the cutting tool at f=2µm.

At a depth of cut a_p=50µm the entire major cutting edge is subject to 'notch' wear with the maximum wear occurring at the intersection of work piece and cutting edge. On the section of the cutting tool which creates the work piece surface the tool profile changes from a continuous radius to something resembling a gothic arc. Given the effect that small edge defects have on surface roughness this is a more favourable wear pattern than notching in this area of the cutting tool.

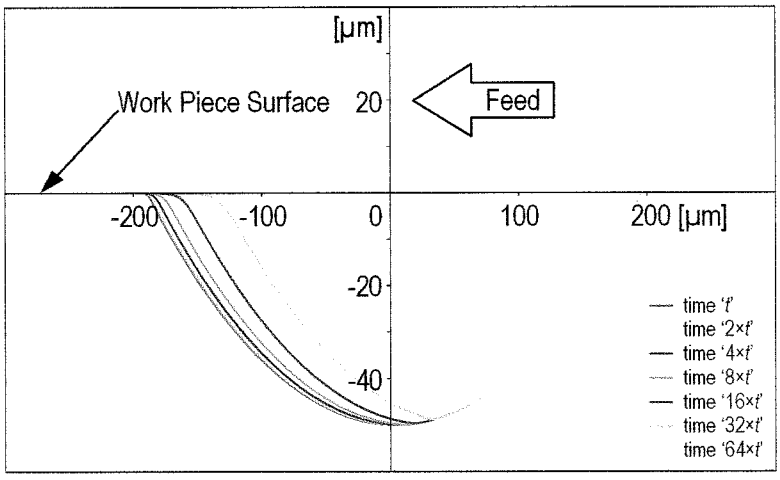

Figure 53: 'Notch' wear at f=2µm

It was postulated earlier [10] that the notch depth could only be as large as the minimum undeformed chip thickness h_{min}. Measurement of notches on hard turning tools show that this is not the case. Actual notch depths at all stages of the tool life depend greatly on feed rate (Figure 54). Notch depths after a cutting time t_c=2min range from 0.67µm for f=10µm to just over 2µm for f=150µm. Note that for reasons described above there are no notch depths given for f=2µm. At the two lower feed rates the notch depth increases initially and then levels off to approximately 1.1µm for f=10µm and 2.4µm for f=40µm. At f=150µm there seems to be a continuous increase in notch depth. However it may be that this notch depth stabilises for cutting times t_c>20min. The largest notch depth recorded for f=150µm is 3.75µm.

Again assuming that the minimum undeformed chip thickness is h_{min}≈1.9µm, then it is now clear that depending on the feed rate the notch depth can be anything from 0.5×h_{min} to 2×h_{min}. This range probably extends even further as a wider range of feed rates and longer cutting times are accounted for.

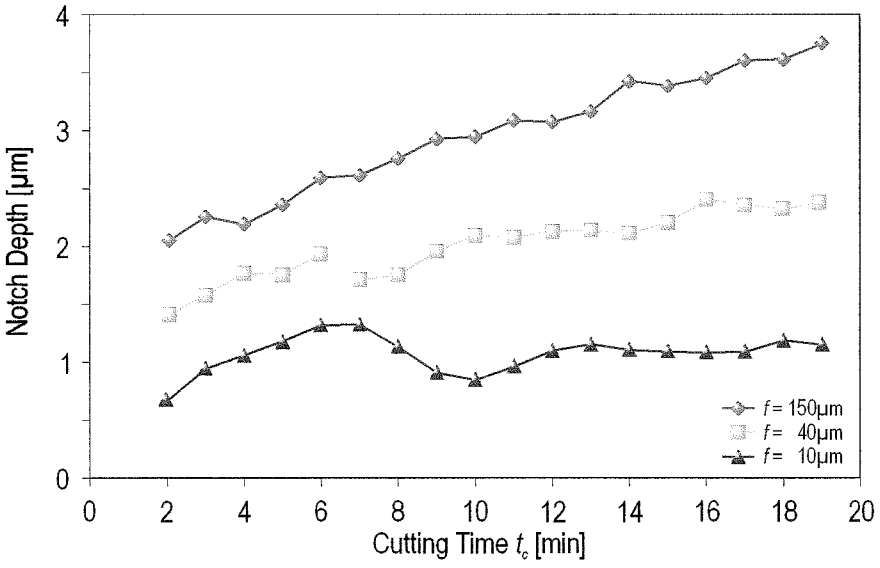

Figure 54: Notch depth development for different feed rates

5.5.3 Effect of tool wear on surface roughness

It is not new that tool wear leads to a degradation of surface roughness. In this chapter an assessment of the causes for this and an estimation of the size of each effect will be attempted. Looking at the development of surface roughness with cutting time (Figure 55) it is clear that the roughness degradation occurs with differing severity and at different times for different feed rates.

Starting with f=2µm the surface roughness remains at around R_a=20nm with variation of some ±10nm. From about t_c=12min a steady rise in roughness can be observed from R_a=20nm to R_a=80-100nm at t_c=19-20min. At the higher feed rate of f=10µm the development of roughness is markedly different. Here the roughness deteriorates steadily right from the start of the measurement, increasing from R_a=45nm to R_a=284nm at t_c=7min. After that time the roughness stabilises and remains in a band of R_a=200-300nm. The Feed rates of f=40µm and f=150µm show a slow but fairly steady increase in roughness over the whole period of the experiment, with a slightly stronger rise in surface roughness during the first quarter of the period.

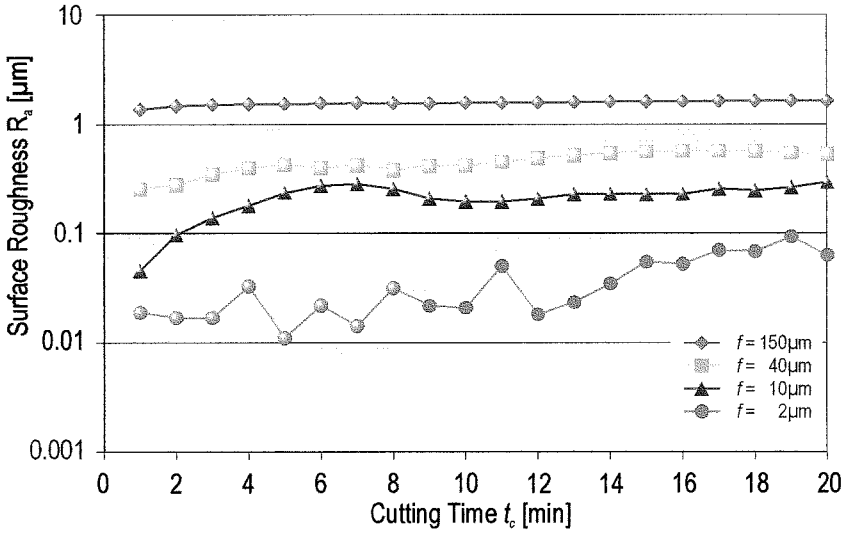

Figure 55: Development of Surface Roughness (R_a) with cutting time

In addition to feed rate the two main factors contributing to surface roughness are tool defect shape and asynchronous vibration. It is therefore necessary to examine the change in these two factors with tool wear. Notch development has already been described in the previous section so the focus now will be on the asynchronous vibration (Figure 56).

The magnitude of the asynchronous vibration again depends strongly on the feed rate. For f=2µm the initial vibration magnitude is 0.1µm, and remains between 0.1µm and 0.2µm for the first ten minutes of cutting. From t_c=10min a rapid rise in vibration can be observed, peaking at 0.43µm for t_c=17min. It is unclear whether the following slightly lower values are random deviations from a continuing rise or in fact a change of behaviour in vibration levels.

Vibration for f=10µm increases more continuously from 0.21µm at t_c=1min to 0.49µm at t_c=20min – even though there are some deviations from a straight line. Both for f=40µm and f=150µm there is no statistically significant rise in vibration over the whole cutting time. The magnitude of vibration ranges from 0.17µm to 0.50µm for these feed rates.

A general trend can be seen in the change of vibration over the cutting time: Initially low feed rates tend to cause less vibration. For high feed rates there is no significant change in vibration, it varies around the same level throughout the first 20 minutes of tool life. In contrast vibration increases at low feeds over the tool life time. The smaller the chosen feed rate the stronger this effect is.

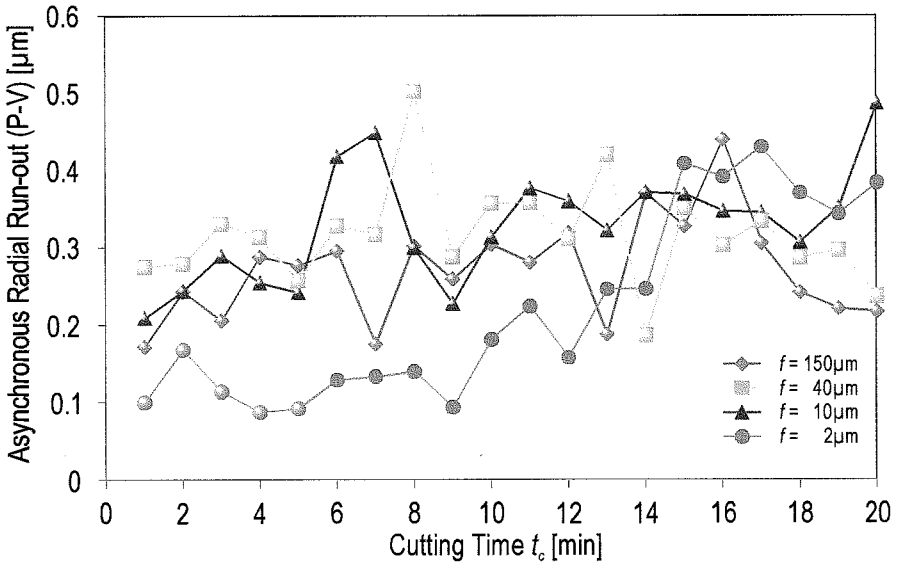

Figure 56: Development of asynchronous vibration with cutting time

With the data for notch size and vibration magnitude for worn tools it is possible to repeat the assessment of the cause and the relative contribution to surface roughness as previously shown in Figure 45. Comparing the data for new and worn tools (Figure 57) it becomes apparent that at the highest feed rate tested (f=150µm) the only relevant contributor to surface roughness is the tool geometry. Neither notching or vibration matter at this feed. As the feed is slowed the tool defect has a stronger effect and this occurs at higher feed rates for worn tools. At f=80µm the effect of tool defects was still very small for new tools. With worn tools it contributes approximately 20% to the roughness at this feed. The tool defects dominate roughness generation for the feed range of f=5µm to 40µm, with neither tool geometry nor vibration contributing greatly to roughness. Reducing feed from f=5µm to f=2µm there is a dramatic change in that vibration increases its contribution from ca. 10% to 90%, or more for worn tools, whereas its contribution to roughness with new tools was only about 70%.

Similar to the observations made on new cutting tools with worn or wearing cutting tools the most important contributor to roughness in the low to medium feed range is the tool defect size, i.e. notching. In addition to the demand for cutting tools of controlled roughness when new, there has to be an emphasis by the machine operator or programmer to utilise cutting strategies which minimise notch wear and therefore reduce the overall tool defect size.

Alternatively it is possible to avoid the problems with tool defects and machining can be carried at very low feed rates. This however will only be successful if the machine vibration can be kept to a minimum. Chatter must be avoided at all costs. It has to be said that machining at f=2µm or slower will remain a choice of last resort at it leads to very long cutting times with low productivity and high tool costs.

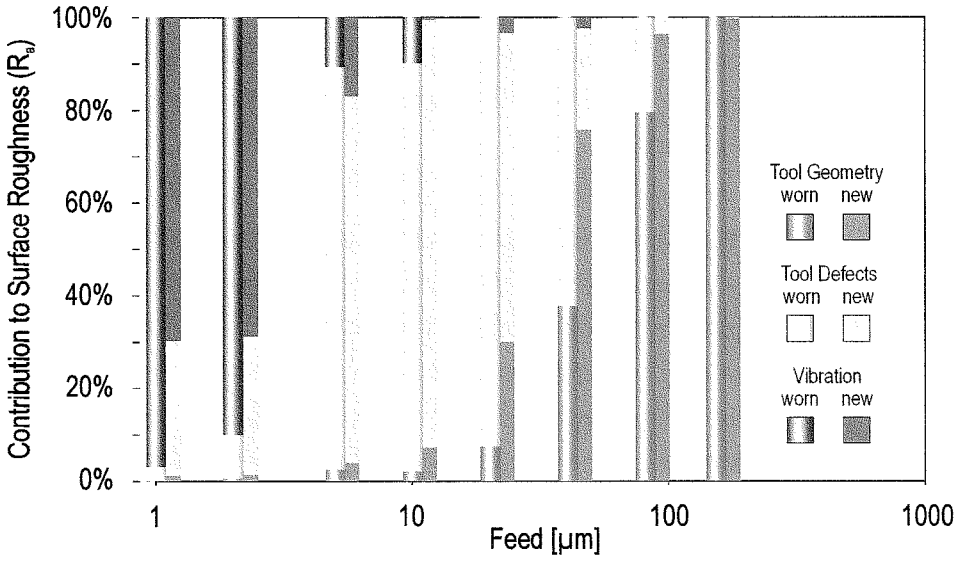

Figure 57: Causes and their relative effects on surface roughness (worn tools)

5.5.4 Conclusions on the material partition equation

In Section 5.2 a simplified material partition equation was defined for the computer simulation and as seen in the previous chapters the equation delivers very useful results in terms of surface roughness prediction. However it still does not address the underlying surface generation mechanisms in a satisfactory manner.

The assumption made previously that in hard turning there is negligible elastic deformation of the work piece surface has been proven by the good correlation between the simulated and measured work piece roughnesses.

The question that still remains is how the two remaining contributing factors change with undeformed chip thickness. The assessment of surface topography and tool profiles of worn cutting tools can give a valuable insight in how these parameters may be distributed. When assessing surfaces generated with worn cutting tools it was shown that those areas of the cutting tool for which the undeformed chip thickness is small are subject to much higher tool wear than the areas where higher undeformed chip thicknesses are encountered. As described above this wear pattern corresponds closely to Brammerz's section of below minimum undeformed chip thickness.

This behaviour must be caused by a significant tribological change occurring in the interaction between tool and work piece in this region and this is responsible for the observed wear pattern. In the past this has been explained with the combined heavy elastic deformation of the cutting tool and work piece material resulting in the accelerated tool wear. However it has just been concluded that in hard turning there is no evidence of elastic deformation. The most likely conclusion is therefore that in hard turning the elastic deformation is replaced by complete plastic deformation of the work piece surface as the undeformed chip thickness falls below the critical threshold value of h_{min}.

This allows now the refinement of the material partition of hard turning as stated in Equation 19 (see also Figure 58). It must be noted that the given material partition is still an approximation of the actual partition occurring in hard turning. It is not certain at this stage that there is no plastic deformation during chip formation and vice versa, also the slope of the transition from plastic deformation to chip removal is as yet uncertain. However the results from the wear tests suggest that the given material partition is an adequate representation of the conditions in the hard turning process.

Equation 19:
$$p_{chip}(h) = \Phi(h - h_{min})$$
$$p_{plastic}(h) = \Phi(h_{min} - h)$$
$$p_{elastic}(h) = 0$$

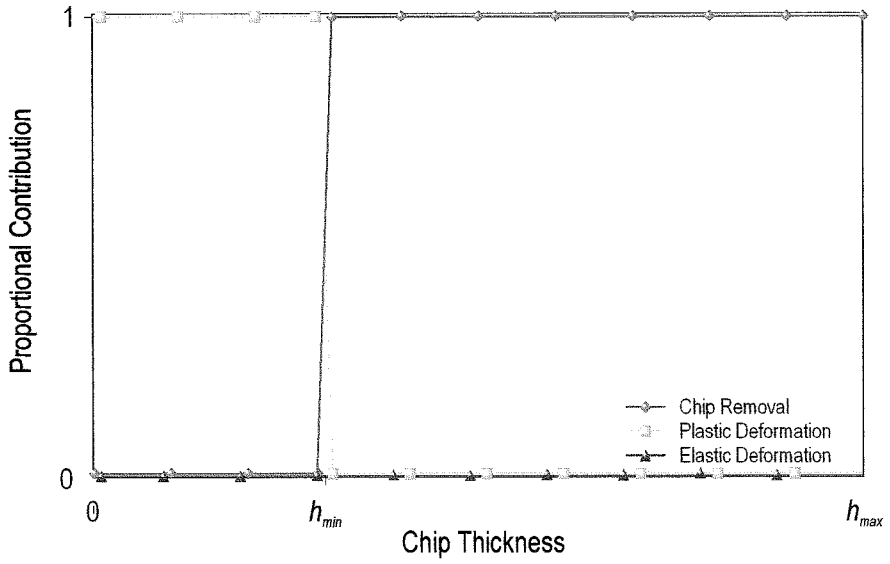

Figure 58: Relative material partition in hard turning

If the above material partition equation is correct then this may have a profound impact on surface integrity in hard turning. In effect a hard turned surfaces generated in this manner will not be generated by one uniform removal mechanism. Instead areas of chip removal will alternate with areas of plastic deformation – in effect a burnishing process – if sectioning the surface in feed direction.

These findings have potentially a very significant effect of surface integrity of hard turned components. The proportion of each feed mark generated by cutting as opposed to burnishing depends on the minimum undeformed chip thickness and the chosen feed rate. This is illustrated by Figure 59 in which simulated surface profiles are plotted for different feed rates. Those areas on the work piece surface that have been generated by plastic deformation are printed with a heavier line weight. For hard turning feeds of f=50µm and above which are typical for industrial applications the areas generated by plastic deformation are fairly small and only take up less than 15% of the machined surface. This changes dramatically as the feed rate is reduced, where more and more of the remaining surface is generated by plastic deformation. At the slowest given feed rate (f=20µm) almost the entire surface (94%) is generated by plastic deformation.

Figure 60 gives a more detailed view of how the proportion of deformation changes with feed rate and cutting edge radius. Looking at the typical edge radius r_n=10µm the plastic deformation for feeds of f≈40µm and above is less than 20%, with an asymptotic approach to 0% for high feed rates. Below the mark of f=40µm the proportion of plastic deformation rises very quickly reaching 100% at a feed rate just under f=20µm. At all feeds smaller than this threshold the complete work piece surface is generated by plastic deformation. This does not mean that no chip removal takes place for these feed rates. The chip removal occurs further forward on the major cutting edge, but subsequent revolutions of the work piece lead to plastic deformation during the generation of the final work piece surface.

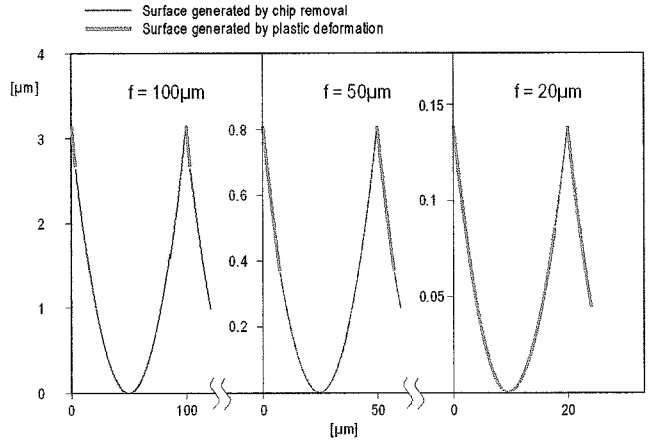

Figure 59: Proportions of plastic deformation on work piece surface (r_ε=0.4mm, r_n=10µm)

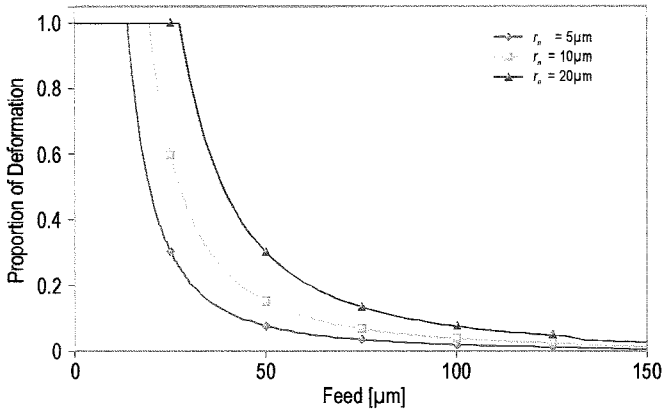

Figure 60: Proportions of plastic deformation with different cutting edge radii (r_ε=0.4mm)

6 CONCLUSIONS AND OUTLOOK

Ultra-precision hard turning is highly deterministic – this is the major conclusion of this thesis. It has been known for some time that turning processes create surface roughness in a way that is accessible to mathematical prediction without a detailed analysis of the precise chip removal process. Past models however had a fundamental shortcoming in that they did not deliver accurate results at low feed rates (with the possible exception of diamond turning).

In developing a new numerical model for surface roughness generation it has now been shown that with the right knowledge about process disturbances, surface roughness and topography can be predicted very accurately. The newly introduced material partition equation, which describes the relative contribution of the material removal mechanisms on the undeformed chip profile, allows the adaptation of the computer simulation to different material removal and deformation conditions.

A large number of cutting trials with a range of feed rates and cutting tools has been carried out to test the model's accuracy. It was found that in addition to standard cutting parameters more inputs are needed for an accurate roughness prediction. Defects on the cutting edge, characterised by their height (or depth) and width, affect surface roughness more than any other input in the medium feed range. At low feeds machine vibration also becomes a significant contributor to roughness.

Once these inputs are included in the model, surface roughnesses can be predicted with very good correlation to the cutting trials. Residual errors are introduced by the uncertainty and variability of the tool defect dimensions. Tool wear on a microscopic scale can change the defect shape and therefore introduce further errors.

Knowing that the variability of the tool defects will be difficult to control in a manufacturing environment, a concept of tool "fingerprints" has been proposed. These fingerprints plot the expected range of surface roughness against feed and take into account the effects of tool defects and machine vibration. They can act as a simple look-up device for machinists and manufacturing engineers to determine the most suitable feed rate for a desired surface roughness. From the fingerprints it is also possible to derive the expected spread of roughnesses, which can be of relevance in the manufacture of surfaces with particular tribological properties.

Tool wear, in particular the occurrence of notch wear, also impacts on surface roughness. As notch wear leads to relatively large defects on the cutting edge it has a potentially detrimental effect on surface roughness. It has been shown that certain ranges of feed are particularly sensitive to this detrimental effect. If machining is to take place at these feeds measures must be taken to minimise notch wear. In some instances it may be necessary to use notch size as a limiting factor on tool life.

From the profiles of worn cutting tools it has been possible to derive an approximate material partition for hard turning. The case seems to be that for undeformed chip thicknesses above a certain threshold chip removal takes place, below the threshold the work piece material is subject to complete plastic deformation. The combination of chip removal and plastic deformation leads to a near perfect imprint of the cutting tool on the work piece surface despite the fact that the transition in mechanism takes place.

If ultra-precision hard turning should become a process that can be applied outside the research laboratory environment several new developments have to be made as follows: The cutting edge quality of hard turning tools needs to be improved to a level which today is only commercially available for monocrystalline diamond tools. In addition to a consistently low cutting edge radius, tool defects need to be reduced significantly. It would be desirable if the defect level was specified and made public by the tool manufacturers so that the machinist can use this data to predict surface roughness.

Further efforts and developments need to be undertaken to reduce notch wear, so that benefits through improvements in the manufacture of hard turning tools are maintained throughout the life of the cutting tool, and are not negated within the first few minutes of life.

Current hard turning machines need to be improved significantly with respect to their dynamic properties. Very high dynamic stiffness and good damping properties are required to counteract the tendency of cutting tools to chatter at low feed rates. In addition to this machine borne vibrations from whatever source need to be reduced similarly to that which is common on ultra-precision diamond turning machines.

It will be some time before ultra-precision hard turning will be widely used to machine optical surfaces. It is likely that cutting tools with the use of finer and finer grain sizes and improved coating technology will eventually become good enough, but whether the economics of the manufacturing process will be competitive against semi-finish hard turning in combination with an appropriate finishing process remains to be seen.

Nevertheless the findings on the effect of edge defect and machine vibration on surface roughness can also be used by manufacturers and users of non-ultra-precision machines. From the data and methods presented it is possible to generate machine/tool fingerprints. These can be applied in utilising existing machine tools to their best potential. Alternatively they can aide machine tool manufacturers to specify an acceptable level of vibration for a particular product and to suit a particular application.

Appendix A Important features on cutting tools

Please refer to [62], [63], [64], [65], [66] for the full range of geometric characteristics of cutting tools.

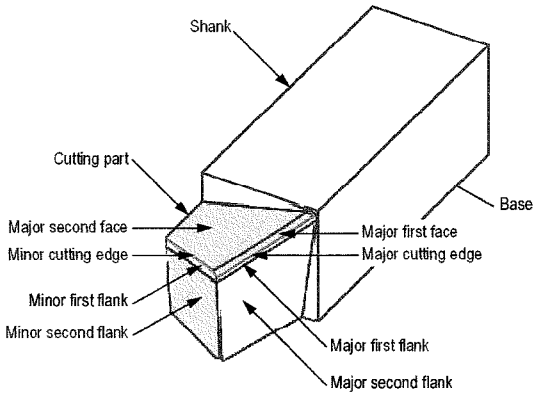

Figure 61: Cutting edges and surfaces on the cutting part of a turning tool

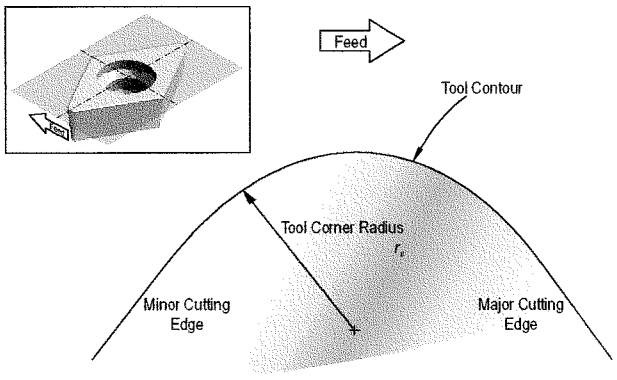

Figure 62: Cutting tool features in the tool reference plane P_r

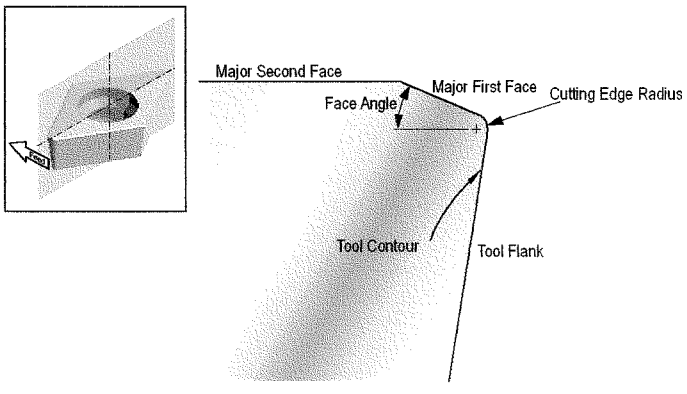

Figure 63: Cutting tool features in the tool back plane

Appendix B Simulation Source Code

```
%surface finish generator

%*********************************************************************
clear all
clc
%initialise indices
i         = 0;
j         = 0;
%*********************************************************************

%*********************************************************************
%set parameters
%all dimensions in microns
Rtool     = 400;    %Tool radius
Angle     = 0.5;    %Wiper angle

DoC  = 50;     %Depth of Cut
Feed = 20;     %Feed per rev

Redge     = 10;     %Cutting edge radius (must be >0 (!))
theta     = 25 *pi/180;
hmin = (1-cos(theta))*Redge

Yserr     = 0.0;    %Serration height
Xserr     = 12;     %Serration spacing

StDevARR  = 0.0;    %standard deviation of Asynchronous Radial Run-out

%*********************************************************************
%new in v3.0:


%*********************************************************************

Delta     = 1.2*sqrt(2*Rtool*DoC+DoC^2);
res  = .05; %horizontal resolution
n         = round(Delta/Xserr)-1;

%*********************************************************************
%create/load tool profile
     path = 'G:\up\Up3910\39101\gen\Experiments\test04_20030117\03_tool_profiles\';
     filename_in = 'tool_210.mat';

          %*********************************************************************
          %Load tool profile from file

          %load(strcat(path, filename_in));
          %toolp(2,:) contains hight data
          %toolp(1,:) contains tool x-coordinates

          %xtool=0:res:max(toolp(1,:)*1000);    %generate x-scale at correct
resolution

          %ztoolloaded = interp1(toolp(1,:)*1000, toolp(2,:), xtool, 'spline')-50;
```

```
        %reverse direction of ztoolloaded (talysurf feedrate measures from right to
        %left) this matlab simulation works from left to right)
        %for i=1:length(ztoolloaded)
            %ztoolloadedr(i)=ztoolloaded(length(ztoolloaded)-i+1);
        %end

        %add empty data range
        %empty =round (Delta/res-0.5*length(ztoolloadedr));
        %ztool = [zeros(1,empty) ztoolloadedr zeros(1,empty)] ;

    %******************
    %alternatively create tool profile
    %normal tool:
    toolp    = toolprofile_simple(Rtool, Delta, res)-DoC;

    %wiper tool:
%   toolp    = toolprofilew(Rtool, Angle, Delta, res)-DoC;

    %***number of centred cos/sin serrations
        x1 =-Delta:res:Delta; %define x coords of serration points
        s_range = -n/2*Xserr:res:n/2*Xserr;
        y_centre =-0.5*Yserr*cos((s_range)/Xserr*2*pi); %define y co-ord.s of
serration points

        y_centre =y_centre - y_centre(1);
        y_left = zeros (round((length(x1)-length(y_centre))/2),1)';
        y_right = zeros ((length(x1)-length(y_centre)-length(y_left)),1)';
        y1 = [y_left y_centre y_right];

        ztool    = toolp+y1; %build ztool with serrations, change +/-y2 for
convex/concave
        %ztool    = toolp-50; %build ztool without serrations


    figure (2)
    plot (ztool)

%************************************************************************
%Machining
%************************************************************************

%generate necessary matrices
%reps = round(1000/Feed+100) %repeat often enough to machine 1000um
reps = 25

mlength = round (1.1*((reps)*Feed+(2*Delta))/res); %determines necessary matrix
length
surface = zeros (mlength,1); %creates initial surface matrix
Aplast = sparse (mlength,1);

%************************************************************************
%Calculate Chip Profile
%************************************************************************

for i=1:reps
    percent_complete = i/reps*100
    %"surface" stores the previously machined surface

    cthick   = zeros (mlength,4);
    %cthick will be used as follows:
```

```
     %stores points p1,p2 and distance d2 in cthick(...):
     %p1 is on surface with co-ordinates (j,surface(j,i-1))
     %p2 is on cutting edge with co-cordinates (k,toolpos(k,i))
     %matrix index -                          (p1x)
     %cthick(:,1)  - surface height value     (p1y)
     %cthick(:,2)  - global position for      (p2x)
     %cthick(:,3)  - cutting edge height value (p2y)
     %cthick(:,4)  - distance between p1 and p2

          offset = StDevARR * randn(1);

     %toolpos stores the tool height data for each revolution
     %(axial position incremented by "Feed")
     startp = round(i*Feed/res);
     endp = startp+length (ztool);
     toolpos = [zeros(1,startp) (ztool+offset) zeros(1,mlength-endp)]';

%subsequent calculations are performed against surface(:,i-1)
%i.e. the previously machined surface
%against toolpos() i.e. the current toolprofile in its (changing) position.

%************************
% determine chip profile
%************************

     % determine start/endpoints where toolprofile is below the w/p surface
     cmp = surface > toolpos ; %generate comparison matrix to find intersection
points
     startj    = min(find(cmp)); %determine hor. start point for outer loop
     endj = max(find(cmp)); %determine hor. end point for outer loop

     %do calculation for each point on surface (index j)
     for j=startj:endj

          %distance checking is only required in a range of +/- hmin,
          %factor 1.1 is probably not required.
          %Thus reduced distance determined by startk/endk
          startk    =j-round(1.1*hmin/res); %determine hor. start point for inner loop
          endk =j+round(1.1*hmin/res); %determine hor. end point for inner loop

          dmin = 10^15; %initialise dmin with large number
          for k=startk:endk
               ind = k-startk+1; %create index starting at 1 (rather than startk)
               d = (surface(j)-toolpos(k))^2+(j-k)^2; %calculate actual distance
                                                      %(square of)
               if d<dmin
                    %if statement saves smallest number encountered for d as dmin
                    %and corresponding k as kmin (x index)
                    dmin=d;
                    kmin=k;
               end %if

          end %k

          %assign numbers
          %j :                    %cthick matrix index (p1x)
          cthick(j,1) = surface(j);    %surface height value (um) (p1y)
          cthick(j,2) = kmin;          %global position (as index figure) for (p2x)
          cthick(j,3) = toolpos(k);    %cutting edge height value (um) (p2y)
          cthick(j,4) = sqrt(dmin);    %distance between p1 and p2 (um)
```

```
    end %for j
%**************************************************************************
%Remove Material
%**************************************************************************

        p1x = (1:mlength)';
        p1y = cthick(:,1);
        p2x = cthick(:,2);
        p2y = cthick(:,3);
        h   = cthick(:,4);

        %material partitions
            Pcut = h>hmin; %Relative material partition in chip

            Pplast = (0<h) & (h<hmin);  %Rel. material partition in plastic def.
            Pelast = 1 - Pplast - Pcut; %Rel. material partition in elastic def.
                                        %not used in calculation

        %Calculate new surface
        surfacex = p1x+(p2x-p1x).*(Pcut+Pplast);
        removaly =     (p2y-p1y).*(Pcut+Pplast);

        removal = interp1(p1x,removaly,surfacex);

        surface = surface+removal;

        Aplastcorr = (Aplast == 1) & (Aplast == (Pcut+Pplast));
        Aplast = Aplast + Pplast - Aplastcorr;
                %store relevant areas of plastic deformation
end %for i

%**************************************************************************
%**************************************************************************

sf_eval = surface;

%crop start of curves
Aplast(1:round((Delta+50)/res)) = [];
sf_eval(1:round((Delta+50)/res)) = [];

%crop end of curves
%Aplast(round (1000/res):length(sf_eval)) = [];
%sf_eval(round (1000/res):length(sf_eval)) = [];

Aplast(round (7*Feed/res):length(sf_eval)) = [];
sf_eval(round (7*Feed/res):length(sf_eval)) = [];


%calculate surface finish parameters
x = (1:length(sf_eval))*res;
m = polyfit (x,sf_eval',0);
l = length (sf_eval);

Rt       = max(sf_eval)-min(sf_eval)
Ra       = mean(abs(sf_eval-m))
Rq       = norm(sf_eval-m)/sqrt(l)
Rsk  = 1/Rq^3/l*(sum((sf_eval-m).^3))

def_prop = sum(Aplast)/length(Aplast)
```

```
%save file
%    save('c:\temp\cthick_out.txt','cthick','-ASCII', '-tabs')
%    save('c:\temp\surface_out.txt','surface','-ASCII', '-tabs')

%highlight plastic deformation in sf_eval
sep_m(:,1) = sf_eval.*not(Aplast);    %area where no plastic removal takes place
sep_m(:,2) = sf_eval.*Aplast;         %area where plastic removal takes place

mask = find(sep_m==0);
sep_m(mask) = NaN;                    %remove 0 values for plotting

sep_m_out(:,1) = x';
sep_m_out(:,2) = sep_m(:,1);
sep_m_out(:,3) = sep_m(:,2);

save('c:\temp\sepm_out.xls','sep_m_out','-ASCII', '-tabs')

figure (1)
plot (x,sep_m(:,1),x,sep_m(:,2),':r')
%plot (x,sf_eval,x,(0.1*Aplast-50))
%annotate plot
minsf = min (sf_eval);
maxsf = minsf +1.5*Rt; %max (sf_eval);
diff = maxsf-minsf;
xpos = 0.05*max(x);
text (xpos,minsf+0.95*diff, strcat ('Corner Rad =', num2str(Rtool)));
text (xpos,minsf+0.9*diff, strcat ('Feed =', num2str(Feed)));
text (xpos,minsf+0.85*diff, strcat ('DoC =', num2str (DoC)));
text (xpos,minsf+0.8*diff, strcat ('Edge Rad =', num2str(Redge)));
text (xpos,minsf+0.7*diff, strcat ('Ra =', num2str(Ra)));
text (xpos,minsf+0.65*diff, strcat ('Rt =', num2str(Rt)));
text (xpos,minsf+0.55*diff, strcat ('Def.Prop.=', num2str(def_prop)));
text (0.8*length(sf_eval), minsf+0.95*diff, '\bf\rightarrow Feed \rightarrow');
axis ([0 max(x) minsf maxsf])
```

References

1 Ng, E.-G., Brazil, D., Monaghan, J., Aspinwall, D.K., A review and analysis of tool/chip interface temperature when machining hardened tool steel with advanced ceramic cutting tools, 32nd international MATADOR conference, Manchester, UK, 1997

2 Tönshoff, H.K., Cutting of hardened Steel. Annals of the CIRP 49/2, Page(s) 547-66. 2000

3 Brandt, D., Randzonenbeeinflussung beim Hartdrehen, Dissertation Universität Hannover, 1995

4 Dubbel: Handbook of Mechanical Engineering, eds. W. Beitz, and K.-H. Kuettner, London: Springer-Verlag. 1994

5 Kaminski, J., Alvelid, B., Temperature reduction in the cutting zone in water-jet assisted turning. Journal of Materials Processing Technology, Page(s) 68-73. 2000

6 Geometrical product specification (GPS) - Surface texture: Profile method - Terms, definitions and surface texture parameters, BS-EN-ISO 4287:2000. 2000

7 Handbook of Surface Metrology, Bristol and Philadelphia: Institute of Physics Publishing. 1994

8 Exploring Surface Texture, 2nd ed., Leicester: Rank Taylor Hobson Ltd. 1986

9 König, W., Klocke, F., Fertigungsverfahren Drehen, Fräsen, Bohren, 6th ed., Springer Verlag. 2002

10 Brammerz, P.-H., Die Entstehung der Oberflächenrauheit beim Feindrehen. Industrieanzeiger, Page(s) 25-32. 1961

11 L'Vov, N.P., Determining the minimum possible chip thickness. Machines & Tooling, Page(s) 45-46. 1968

12 Schmidt, J., Mechanische und thermische Wirkungen beim Drehen gehärteter Stähle, Dissertation Universität Hannover, 1999

13 Ikawa, N., Shimada, S., Tanaka, H., Ohmori, G., An atomistic analysis of nanometric chip removal as affected by tool-work interaction in diamond turning. Annals of the CIRP 40/1, Page(s) 551-54. 1991

14 Aspinwall, D.K., Ng, E.G., Schnittkraft und Temperatur beim Hartdrehen von gehärtetem Gesenkstahl. Industrie Diamanten Rundschau, Page(s) 260-273. 1999

15 Klimenko, S.A. *et al.*, On the Wear Mechanisms of Cubic Boron Nitride Base Cutting Tool. Wear. 1992

16 Matsumoto, Y., Magda, D., Hoeppner, D.W., Kim, T.Y., Effect of machining processes on the fatigue strength of hardened AISI 4340 steel. Journal of Engineering for Industry, Transactions of the ASME, Page(s) 154-59. 1991

17 Griffiths, B.J., Furze, D.C., Tribological advantages of white layers produced by machining. Journal of Tribology, Transactions of the ASME, Page(s) 338-42. 1987

18 Bongardt. J., Werner, A., Beeinflussung der Werkstoffstruktur in der Randzone beim Drehen mit CBN. Fertigungstechnik und Betrieb, Page(s) 353-54. 1990

19 Matsumoto, Y., Barash, M.M., Liu, C.R., Effect of hardness on the surface integrity of AISI 4340 steel. Journal of Engineering for Industry, Transactions of the ASME, Page(s) 169-75. 1986

20 Liu, C.R., Barash, M.M., The Mechanical State of the Sublayer of a Surface Generated by Chip Removal Process. Part 1: Cutting with a sharp tool. Journal of Engineering for Industry, Transactions of the ASME, Page(s) 1192-208. 1976

21 Jochmann, S., Untersuchungen zur Prozess- und Werkzeugauslegung beim Hochpraezisionshartdrehen, Dissertation Aachen, Aachen, 2001

22 Matsumoto, Y., Hashimoto, F., Lahoti, G., Surface integrity generated by precision hard turning. Annals of the CIRP 48/1, Page(s) 59-62. 1999

23 König, W., Berktold, A., Koch, K.-F., Turning versus grinding-a comparison of surface integrity aspects and attainable accuracies. Annals of the CIRP 42/1. 1993

24 Fleming, M.A., Sweeney, M.A., Valentine, T.J., Simpkin, R., PCBN hard turning and workpiece surface integrity. Industrial Diamond Review. 1998

25 Neailey, K., Surface integrity of machined components-residual stresses and fatigue. Metals and Materials, Page(s) 141-45. 1988

26 Brinksmeier, E. *et al.*, Residual Stresses - Measurement and causes in machining processes. Annals of the CIRP 31/2, Page(s) 491-510. 1982

27 Product Information Seco Tools (U.K.) Ltd..

28 Product Information Sumitomo Electric Hardmetal.

29 Product Information Sandvik Coromant UK.

30 Knüfermann, M.M.W. *et al.*, Ultra-precision turning of hardened steel with Amborite DBN45 of the DeltaTurn40 lathe. Industrial Diamond Review, Page(s) 107-14. 2000

31 Davies, M.A., Chou, Y.K., Evans, C.J. , On chip morphology, tool wear and cutting mechanics in finish hard turning. Annals of the CIRP 45/1, Page(s) 77-82. 1996

32 Chou, Y.K., Evans, C.J., Tool wear mechanism in continuous cutting of hardened tool steels. Wear, Page(s) 59-65. 1997

33 Chou, Y.K., Evans, C.J., Microstructural effects in precision hard turning , Proceedings of the 1996 ASME International Mechanical Engineering Congress and Exposition , Page(s) 237-242 Atlanta, GA, USA , 1996

34 Abele, E., Sham, E., Schulz, H., Wear Mechanism when Machining Compacted Graphite Iron. Annals of the CIRP 51/1, Page(s) 53-56. 2002

35 Internal Report Cranfield Precision.

36 Penalva, M.L., Arizmendi, M., Diaz, F., Fernandez, J., Effect of tool wear on roughness in hard turning. Annals of the CIRP 51/1, Page(s) 57-60. 2002

37 Merchant, M.E., Mechanics of the Metal Cutting Process. I. Orthogonal Cutting and a Type 2 Chip. Journal of Applied Physics, Page(s) 267-75. 1945

38 Lee, E.H., Shaffer, B.W., The Theory of Plasticty applied to a problem of machining. Journal of Applied Mechanics, Page(s) 405-12. 1951

39 Elbestawi, M.A., Srivastava, A.K., El-Wardany, T.I., A Model For Chip Formation During Machining of Hardened Steel. Annals of the CIRP 45/1, Page(s) 71-76 . 1996

40 Mamalis, A.G., Branis, A.S., Manolakos, D.E., Modelling of precision hard cutting using implicit finite element methods. Journal of Materials Processing Technology, Page(s) 464-75. 2002

41 Guo, Y.B., Liu, C.R., 3D FEA modeling of hard turning. Journal of Manufacturing Science and Engineering, Page(s) 189-99 . 2002

42 Kelly, K., Young, P., Byrne, G., Modelling the influence of machining dynamics on surface topography in turning. International Journal of Mechanical Sciences, Page(s) 507-26. 1999

43 Chou, Y.K., Evans, C.J., White layers and thermal modeling of hard turned surfaces. International Journal of Machine Tools and Manufacture, Page(s) 1863-81. 1999

44 Taniguchi, N., Current Status in, and Future Trends of Ultraprecision Machining and Ultrafine Materials Processing. Annals of the CIRP 32/2, Page(s) 573-82. 1983

45 Brinksmeier, E., Preuss, W., Gläbe, R., Single Point Diamond Turning of Steel, Proceedings of the euspen 1st international conference, Page(s) 446-449 Bremen, Germany, 1999

46 Brinksmeier, E., Gläbe, R., Advanced cutting tools for precision machining of steel, Proceedings of the euspen 2nd international conference, Page(s) 628-631 Turin, Italy, 2001

47 Moriwaki, T., Shamoto, E., Ultraprecision diamond turning of stainless steel by applying ultrasonic vibration. Annals of the CIRP 44/1, Page(s) 559-62. 1991

48 Moriwaki, T., Shamoto, E., Ultrasonic Elliptical Vibration Cutting. Annals of the CIRP 45/1, Page(s) 31-34. 1995

49 Shamoto, E., Moriwaki, T., Ultraprecision diamond cutting of hardened steel by applying elliptical vibration cutting. Annals of the CIRP 48/1, Page(s) 441-44. 1999

50 Stephenson, D.J., Corbett, J., Sweet, J.H., Tetraform 'C'- A major advancement in the efficient machining of optical surfaces on hardened steels, Proceedings of the euspen 2nd international conference, Turin, Italy, 2001

51 Stephenson, D.J., Veselovac, D., Manley, S., Corbett, J., Ultra-precision grinding of hardened steels. Precision Engineering, Page(s) 336-45. 2001

52 Ball, M.J., Murphy, N.A., Shore, P., Electronically assisted "ductile" mode diamond grinding of BK7 and SF10 optical glass. Proceedings of the SPIE. 1992

53 Carlisle, K., Fitzpatrick, J., McKeown, P.A., Shore, P., Review of the Ultra Precision Machining Research Facility - the "NION" Machine. Internal Report Cranfield Precision.

54 Wills-Moren, W.J., Carlisle, K., McKeown, P.A., Shore, P., Ductile regime grinding of glass and other brittle materials by the use of ulta-stiff machine tools. Proceedings of the SPIE, Page(s) 126-35. 1990

55 Carlisle, K., Pierse, M.G., Manley, S., High precision manufacturing cell for motor bearing components. IEEE Transactions on Magnetics, Page(s) 963-67. 1999

56 Clarke, M., Manley, S., Pierse, M.G., A Unique Ultra-Precision Lathe for the Hard and Soft Turning of Precision Components, Proceedings of the 1st International euspen Conference, Bremen, 1999

57 Bryan, J.B., The Abbe Principle Revisited: An Updated interpretation. Precision Engineering, Page(s) 129-32. 1979

58 Kishawy, H.A., Elbestawi, M.A., Effects of process parameters on material side flow during hard turning. International Journal of Machine Tools and Manufacture, Page(s) 1017-30. 1999

59 Nishiguchi, T., Masuda, M., Mirror-Like Cutting Of Ferrous Metals With CBN Tools, Proceedings of the 14th North American Manufacturing Research Conference, Page(s) 459-464 1986

60 Axes of Rotation, Methods for Specifying and Testing, ANSI/ASME B89.3.4M. 1985

61 Bryan, J.B., The Deterministic Approach in Metrology and Manufacturing, International Forum on Dimensional Tolerancing and Metrology , Dearborn, Michigan, 1993

62 Basic quantities in cutting and grinding - Part 1: Geometry of the active part of cutting tools - General terms, reference systems, tool and working angles, chip breakers, ISO 3002-1:1982/ Amd 1:1992. 1992

63 Basic quantities in cutting and grinding - Part 1: Geometry of the active part of cutting tools - General terms, reference systems, tool and working angles, chip breakers , ISO 3002-1:1982. 1982

64 Basic quantities in cutting and grinding - Part 2: Geometry of the active part of cutting tools - General conversion formulae to relate tool and working angles, ISO 3002-2:1982. 1982

65 Basic quantities in cutting and grinding - Part 3: Geometric and kinematic quantities in cutting, ISO 3002-3:1984. 1984

66 Basic quantities in cutting and grinding - Part 4: Forces, energy, power, ISO 3002-4:1984. 1984